DIPLOMARBEIT
MASTER'S THESIS

Failure modes of wood cells identified by an approach based on the extended Finite Element method

ausgeführt zum Zwecke der Erlangung des akademischen
Grades eines Diplom-Ingenieurs

unter der Anleitung von

Univ.-Ass. Dipl.-Ing. **Markus Lukacevic**
Institut für Mechanik der Werkstoffe und Strukturen
Fakultät für Bauingenieurwesen
Technische Universität Wien

Univ.-Ass. Dipl.-Ing. Dr. techn. **Josef Füssl**
Institut für Mechanik der Werkstoffe und Strukturen
Fakultät für Bauingenieurwesen
Technische Universität Wien

und

Univ.-Prof. Dipl.-Ing. Dr. techn. **Josef Eberhardsteiner**
Institut füur Mechanik der Werkstoffe und Strukturen
Fakultät für Bauingenieurwesen
Technische Universität Wien

eingereicht an der Technischen Universität Wien
Fakultät für Bauingenieurwesen

von

Ralf Lampert

Matr.Nr.: 02 26 264
Erlengasse 13
A - 6890 Lustenau

Wien, im März 2014

Danksagung

Diese Diplomarbeit stellt den Abschluss meines Diplomstudiums an der Technischen Universität Wien dar. An dieser Stelle möchte ich mich bei allen bedanken, die zu meinem Studium und dieser Arbeit beigetragen haben, und ohne die ich dieses abschließende Ziel nicht erreicht hätte.

Für die ausgezeichnete Betreuung und genaue Korrektur meiner Diplomarbeit danke ich Herrn Univ.- Ass. Dipl.-Ing. Markus Lukacevic und Herrn Univ.- Ass. Dipl.-Ing. Dr. techn. Josef Füssl recht herzlich. Sowohl sie als auch die gesamten Mitglieder der Holzgruppe am Institut für Mechanik der Werkstoffe und Strukturen standen jederzeit für Fragen und Hilfestellungen zur Verfügung.

Abschließend sei Univ.- Prof. Dipl.-Ing. Dr. techn. Josef Eberhardsteiner gedankt, dass er mir diese Diplomarbeit ermöglicht hat.

Abstract

Wood is a natural material enjoying high popularity as structural element for different building constructions, due to its good processability, carrying capacity, thermal insulating effect and energy balance. Since the demands on structural elements are increasing constantly and to remain the competitiveness of wood against other building materials, design concepts for wooden elements must also evolve continuously. For that, a detailed characterization of the mechanical behavior of wood, from the elastic range up to plastic effects and failure, is necessary.

The motivation of this thesis is to contribute to a better understanding of the failure modes observed in wooden structures. The initiation as well as direction of cracks is strongly triggered by the microstructure of wood. For this reason, a multi-scale approach consisting of three scales of observation was chosen. Typical cell structures of early- and latewood represent the lowest scale, followed by the next higher scale consisting of homogeneous early- and latewood layers, and finally the homogeneous clear wood material at the highest level. Within this thesis the main focus is laid on the early- and latewood cell structures.

Two unit cells were developed and a model based on the Finite Element method is used to determine crack initiation and the corresponding crack directions. A wood cell consists of numerous layers, whereas the middle lamella and the so-called *S2* layer mainly affect crack initiation and the cracking mode. Thus, only these two layers were considered within the developed unit cells. The middle lamella is assumed to exhibit an isotropic material behavior and a Drucker-Prager failure criterion is assigned. The *S2* layer behaves tranversal isotropic and also failure initiation as well as the crack directions are defined by taking the material orientation into account.

By applying periodic boundary conditions and different load combinations to the unit cells, failure surfaces for different stress relationships could be obtained. Moreover, different failure modes were identified and assigned to stress spaces, providing a basis for the determination of crack directions at the clear-wood scale. Finally, the well-known anisotropic Tsai-Wu failure criterion, often applied to wood and wood-based products, was compared to the numerically obtained failure surfaces.

Kurzfassung

Holz ist ein natürlicher Baustoff, der sich als strukturelles Element für verschiedenste Konstruktionen aufgrund seiner guten Verarbeitbarkeit, Tragkapazität, thermisch isolierenden Wirkung und Energiebilanz großer Beliebtheit erfreut. Da die Nachfrage an strukturellen Elementen steigt und um die Wettbewerbsfähigkeit von Holz gegenüber anderen Baustoffen zu gewährleisten, ist es notwendig Bemessungskonzepte für Holz konstant weiterzuentwickeln. Dafür ist eine detaillierte Charakterisierung des Materialverhaltens von Holz, angefangen vom elastischen Bereich bis hin zu plastischen Effekten und Versagen, notwendig.

Der Beweggrund für diese Arbeit ist es, einen Beitrag zu einem besseren Verständnis der Versagensmechanismen, die in Holzstrukturen beobachtet werden, zu leisten. Sowohl die Rissentstehung als auch die Richtung der Risse werden stark von der Mikrostruktur des Holzes beeinflusst. Aufgrund dessen wurde ein Mehrskalenansatz bestehend aus drei Längenskalen gewählt. Typische Zellstrukturen von Früh- und Spätholz stellen die niedrigste hierarchische Skalierung dar, darauf folgt die nächsthöhere Skalierungsebene bestehend aus homogenen Früh- und Spätholzschichten und schlussendlich das homogene Material Holz als höchste hierarchische Ebene. Der Fokus dieser Arbeit liegt auf den Früh- und Spätholzzellstrukturen.

Zwei Einheitszellen wurden entwickelt und ein Modell zur Bestimmung der Rissbildung und der entsprechenden Rissrichtungen basierend auf der Finite Elemente Methode angewandt. Eine Holzzelle besteht aus zahlreichen Schichten, wobei hauptsächlich die Mittellamelle und die sogenannte *S2*-Schicht die Rissbildung und die Art des Risses beeinflussen. Folglich wurden lediglich die o.g. Schichten bei der Entwicklung der Einheitszelle berücksichtigt. Es ist anzunehmen, dass die Mittellamelle, der ein Drucker-Prager Versagenskriterium zugewiesen wurde, ein isotropisches Materialverhalten aufweist. Die *S2*-Schicht verhält sich transversal isotropisch und sowohl die Rissbildung als auch die Rissrichtung sind durch die Berücksichtigung der Materialorientierung definiert.

Durch die Anwendung von periodischen Randbedingungen und verschiedenen Lastkombinationen an der Einheitszelle, können Versagensflächen für unterschiedliche Spannungskombinationen bestimmt werden. Zusätzlich wurden unterschiedliche Versagensfälle identifiziert und ihren Spannungsbereichen zugeordnet. Dies stellt die Basis für die Bestimmung der Rissrichtungen auf der Vollholzlängenskala dar. Schlussendlich wurde das bereits bekannte anisotropische Wu Versagenskriterium, welches meist für Holz und holzbasierende Produkte angewendet wird, mit der numerisch erhaltenen Versagensfläche verglichen.

Contents

Nomenclature

Abbreviations

FEM	Finite Element method
XFEM	eXtended Finite Element method
EW	earlywood
LW	latewood
UC	unit cell
ML	middle lamella
P	primary cell wall
S1	first layer of secondary wall
S2	second layer of secondary wall
S3	third layer of secondary wall
MFA	microfibril angle
L	longitudinal direction
R	radial direction
T	tangential direction

Symbols

L,R,T	Local material directions
X,Y,Z	Global Cartesian coordinate system
μ	Coefficient of friction
ν	POISSON's ratio
τ	Shear stress
$\boldsymbol{\sigma}_{rot}$	Roted stress tensor
$\boldsymbol{\sigma}$	Stress tensor
$\boldsymbol{\varepsilon}$	Strain tensor
$\boldsymbol{\varepsilon}^p$	Plastic strain tensor
$\mathbb{C}$	Stiffness matrix
$\mathbb{D}$	Compliance matrix
a,b	TSAI-WU coefficients
f_c	Compression strength
f_t	Tensile strength
f_v	Shear strength
u	Displacement
RF	Reaction Force
E	Young's modulus of elasticity
G	Shear modulus
E_L	Young's modulus in fiber direction
E_R	Young's modulus in radial direction
E_T	Young's modulus in tangential direction
E^{MMM}	Young's modulus obtained from the macromechanical model

Chapter 1

Introduction

1.1 Motivation

The application of numerical simulation tools like the Finite Element method for a realistic and reliable analysis of plates and shells made of wood, as well as the investigation of the spatial deformation behavior of biaxially stressed components made of wood requires the availability of suitable material laws.

At the present time several material models for the description of the mechanical behavior of wood exist. The most simple ones consider merely elastic behavior, with or without the typical orthotropy of wood. To be able to determine strength properties of wood numerically, these models have to be extended for example, by allowing perfect plastic behavior by using failure criteria like the one proposed by Tsai and Wu [22]. These approaches allow the redistribution of stresses to a certain extent, but are not able to describe the initiation and propagation of cracks. To overcome this deficit, within this thesis, a modelling strategy for a failure criterion which allows the consideration of cracks was developed.

Hence, to develop a failure criterion, the structural features of all length scales should be taken into account, reaching from the layered structure of the wood cell wall, to the honeycomb-like structure of the wood cells, and finally up to the layered structure of early- and latewood, known as annual rings.

More precisely, such a failure criterion shall lead to a proper calculation model for all kinds of wood and wood composites. In this specific case, this thesis and its research findings should contribute to a complex material model for spruce, which will be used at the IMWS (Institute for Mechanics of Materials and Structures, Vienna University of Technology).

With the existence of a material model for wood, including the anisotropic failure criterion with crack propagation, all of the wood composites can be evaluated with the Finite Element method more accurately and therefore more efficiently.

The material wood is considered as a homogeneous material, based on works of Keylworth [11] and Kollmann [12], where the mechanical behavior is described within the framework of the generalized Hooke's law. Based on Eberhardsteiner [6], the parameters for the Tsai and Wu [22] failure criterion of biaxial loaded spruce were obtained. Since this publication, it has been the state-of-the-art failure criterion for the description of failure initiation of wood. However, crack propagation and crack directions are not considered in detail.

At the IMWS, several prior studies have dealt with the numerical formulation of a material model for wood. Some of these papers influenced this thesis as named in this chapter. Material characteristic values for the numerical Finite Element analysis used in this thesis, e.g. stiffnesses and strengths, have been adopted from the researches of Bader [2]. Bader researched the structure of wood and identified the properties of the components as lignin, cellulose or hemicellulose.

The work of Mishnaevsky Jr. [17] describes the micromechanical modelling of mechanical behavior and strength of wood. It presents an overview of the micromechanical theoretical and numerical models of wood. The differentiation in mesoscaled (cellular models) and microscaled (laminate models) is made, and the combination of these two models (multiscale models) is analysed as well. Thus, it is evident that this model allows consideration of the structures of wood at both meso and micro levels. His idealized geometry of a honeycomb-like structured cell could be adopted for the geometry used in this thesis. The design of the unit cell could be adopted from the thesis of Gloimüller [8], who had developed the formation of the geometry of cells based on the density of wood. From the work of Eberhardsteiner [6] the biaxial strength of spruce could be adopted, which served as verification for the numerical simulation tool (see chapter 2).

The fibre matrix failure criterion for cellulose fiber reinforced lignin was adopted from Puck [19, 20], which was used for the examination of the unit cell parts in the numerical models. The impact of the reinforced fiber directions on the unit cells' Finite Element model was adopted from Deng [5]. In Deng's work it is shown how the micro fibril angle (MFA) affects the model's mechanical behavior.

On the basis of the formulation of the *Periodic Boundary Conditions* [18], all analysis could be conducted on a unit cell.

1.2 Scope

The aim of this thesis is to develop a concept for the description of crack initiation and, especially, propagation in wood, which should be implemented in a previously developed numerical simulation tool for wooden boards [14].

The application of common failure criteria for orthotropic materials can be used to identify the start of cracking, but for the further crack propagation knowledge about the global crack direction is inevitable.

A closer look into the material wood reveals several structural features on different length scales. Thus, to obtain the global crack direction, a multiscale damage approach was taken. First, the failure mechanisms at the single cell level were identified for early- and latewood cells, respectively, to obtain the crack direction for several loading conditions at the lowest length scale by using the unit cell method in combination with the eXtended Finite Element method (XFEM). In a next step, these results will be combined at the annual ring level, where early- and latewood cells form a layered structure. This finally leads to predefined global crack directions for varying loading conditions, which will be implemented in a subroutine of the commercial FE software *Abaqus™*.

Within this thesis, the focus lied on the first step of the multiscale approach, the single cell level. At this level, the cells have a constant shape in longitudinal (L) direction, whereas pronounced differences in radial (R) and tangential (T) direction, respectively, can be noticed. Thus, an emphasis was put on the investigation of the RT-plane.

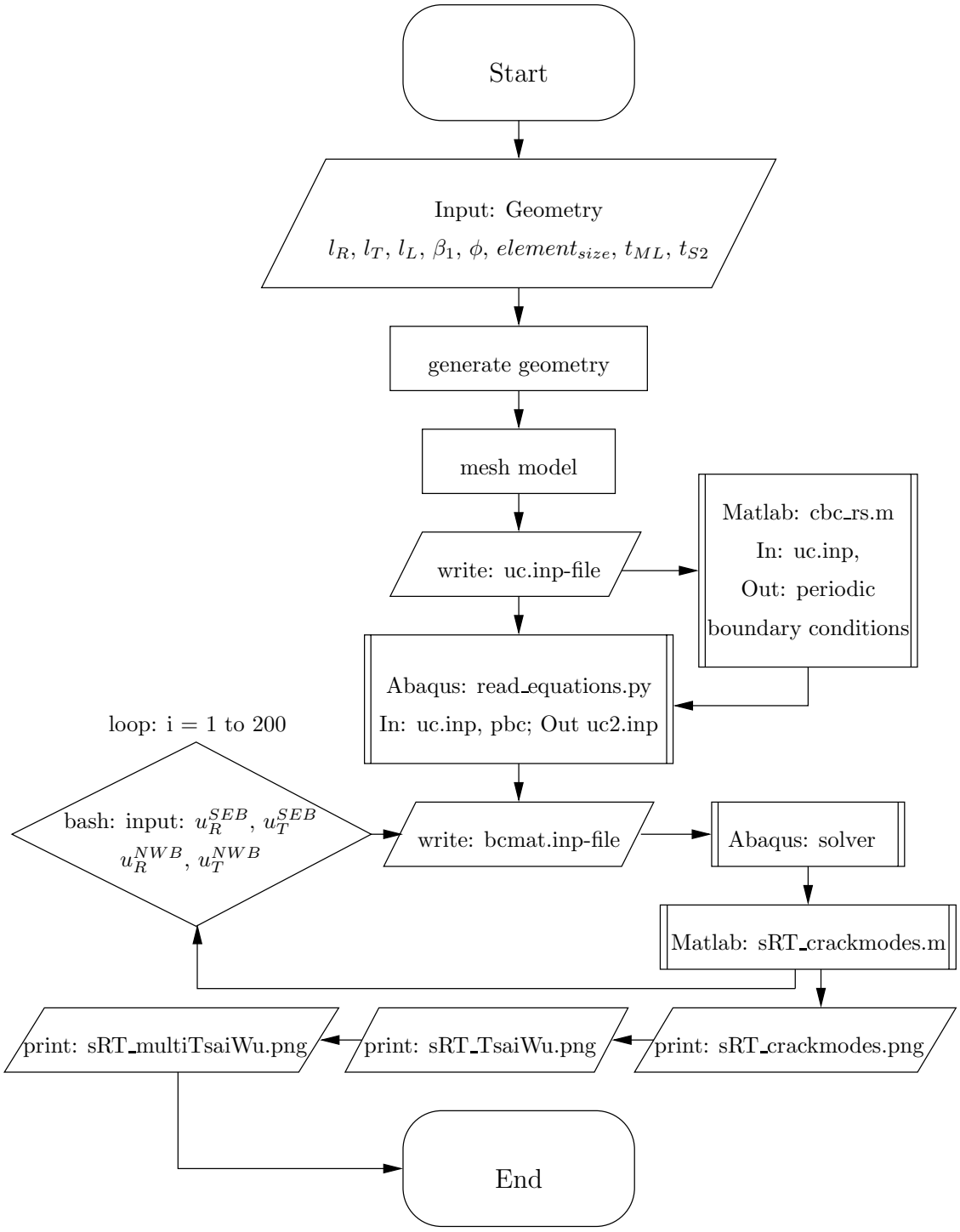

Figure 1.1: Flowchart, showing the complete procedure of the generation and evaluation

The flowchart in Figure 1.1 shows the complete procedure of the evaluation of the failure criteria. The first step is to define the geometry input parameters for the *Abaqus™* python input file, explained in subchapter 2.2.1, which leads to a *Abaqus™* input file, containing the node, element and material definitions

but lacking the boundary conditions and loadings.

In the second step a *Matlab™* script imports this previously generated input file and calculates the periodic boundary conditions by formulating a constrained equation for each node and its corresponding node.

These generated equations are reintegrated into the prior generated *Abaqus™* input file. A completed *Abaqus™* input file, including all necessary information, can be generated by means of an additional python script.

The next tasks are implemented as a loop in terms of defining the load, calculating the previously generated numerical model and evaluating the crack initiation and crack propagation for 200 different load cases, i.e. 200 times for each of both cell types.

After completion of this loop, the evaluated data is aggregated to one total failure criterion for each cell type.

1.3 Structure and Content

This thesis is organized in three chapters. Chapter 2 presents the thematic introduction, containing the material mechanical principles. The numerical model and its structure containing the materials and material properties of the used cell layers, which were developed within the scope of this thesis, are presented in Chapter 2 as well. Chapter 2 is furthermore divided in three subchapters, starting with a short introduction of the numerical simulation tool and its objectives. The second subchapter addresses unit cells, their composition is explained by means of their geometry and two different layers. Based on each of these two layers the used specific material values and crack criteria are explained. The last part of this chapter shows the Finite Element model, regarding mesh fineness, boundary conditions and applied loads.

Other significant aspects are the crack propagation and crack development within the earlywood and latewood cells, which are issued in Chapter 3. This chapter, the last part of this thesis, deals with the calculation of all load combinations and the evaluation of the resulting data. It is divided into four subchapters, the first subchapter addresses the different loadcases, the second subchapter addresses the results received from calculations from the earlywood cells and the results from the latewood cells. The equal structure of these two subchapters is described hereafter. Both start with a description of all treated loadcases and their evaluation, which leads to a collection of all cracking points and its associated results of the respective unit cell, represented in σ_{RR} - σ_{TT} stress plane. On the basis of this pooled analysis of stress states, it will be possible to evaluate the best fitting Tsai - Wu parameters. Since the Tsai - Wu failure criterion is an illustration of an ellipsoid, it will be more precise to use multiple Tsai - Wu criteria, the so-called multi-surface failure criterion.

The third chapter contains the summary and conclusions including the interpretation of all data generated in Chapter 2. To prove this thesis' ability to

generate an entire failure criterion, a comparison of the generated macroscopic elastic limit with the macroscopic values of spruce depicted by HOFSTETTER et al. [9] was done. Furthermore, a comparison of the obtained failure criteria for early- and latewood with the well-known anisotropic failure criterion of TSAI-WU was done. The Appendix contains a perspective to future work. Further, the collected findings are presented in the summary and an outlook to future work is given.

Chapter 2

Numerical Simulation Tool

In this chapter all the necessary models for the description of the material behavior of the wooden cells are presented. Additionally, the mechanical parameters, which were used as input for the numerical simulation tool, are shown. For the simulation, the commercial software *Abaqus™* was used. This software also allows for the consideration of discrete cracks and the crack propagation through the eXtended Finite Element Method (XFEM).

A proper numerical model is built up of three components: the basic model with its material definitions, boundary conditions and loads.

The assembly of the model is divided into several steps, starting with an input script for *Abaqus™*, written in python scripting language. Based on the input parameters of the geometry the unit cell is generated automatically, followed by the allocation of sections and materials.

Another component of the Finite Element model are the boundary conditions. In this specific case of a unit cell these boundary conditions were formulated as *Periodic Boundary Conditions*, described more precisely in Chapter 2.3. A *Matlab™* script was used to formulate these constrained boundary conditions between nodes and their corresponding nodes.

To be able to identify critical stress states, the loads have been applied with prescribed displacements.

In order to obtain the best possible distribution of stresses, which will lead to cracks, the displacements were applied parallel and perpendicular to the symmetry plane, which corresponds to tension, pressure or shear loads. This considerably high amount of load combinations was applied fully automatically on the model, which was created in advance, and was evaluated fully automatically by means of bash scripts.

After finishing all calculations, a combined analysis of the unit cell stresses up to cell failure was made with *Matlab™*.

2.1 Introduction

Wood is a naturally grown, organic material and consisting of lignin, cellulose and hemicellulose. It is highly inhomogeneous and porous. Two different parts of wood can be distinguished, namely earlywood and latewood, because the growth activity of trees varies within a year. Wood is an anisotropic material because of its cell structure, for this purpose there are widely differing mechanical properties in longitudinal, transversal and radial direction of a log.

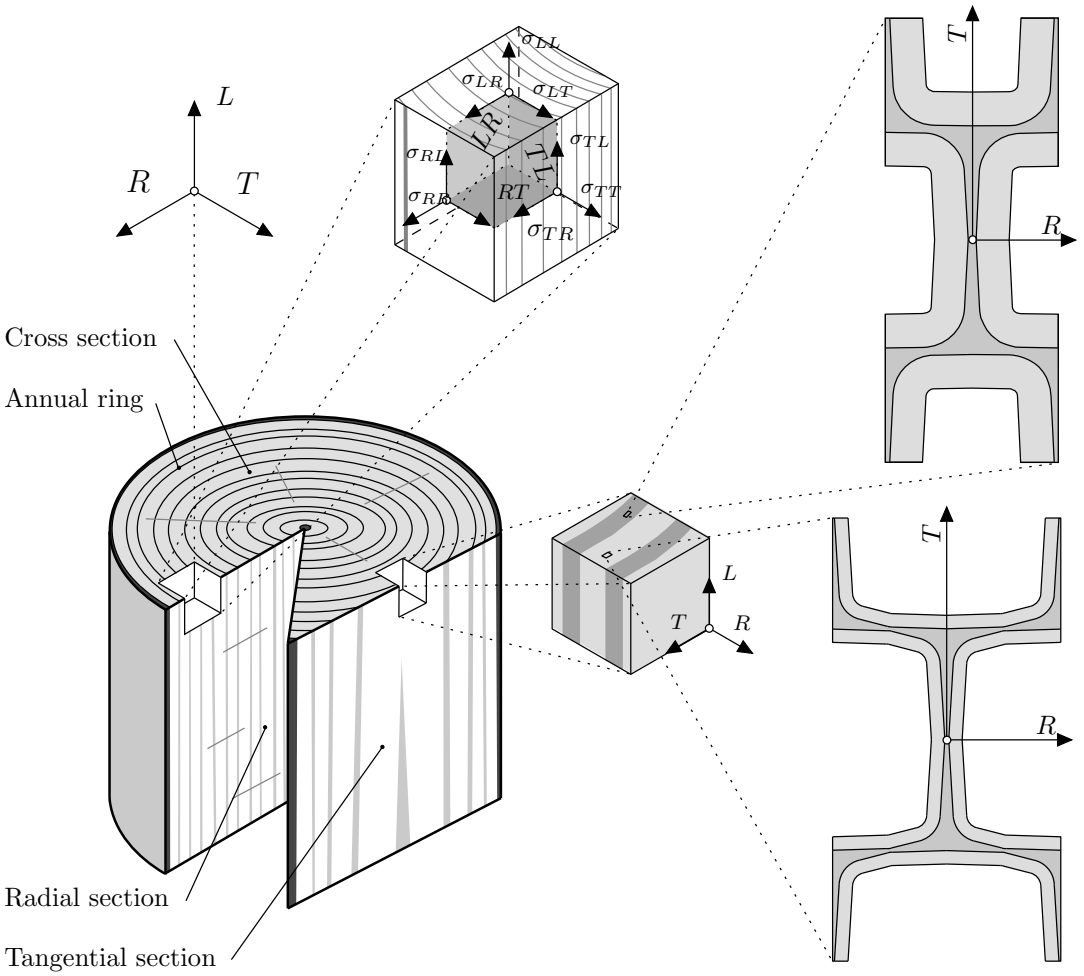

Figure 2.1: Sections of a log, primary material directions and its unit cells

Figure 2.1 shows the wooden log at a macroscopic scale and its annual rings. The local coordinate system for the homogenized clear wood material and the notation of stress components is also given. In addition, Figure 2.1 shows the abstraction of the two different unit cells out of the annual rings.

To be able to describe the cracking behavior at the macroscopic level, first, the cracking behavior at the cell wall level should be understood. For this, the unit cell method was introduced.

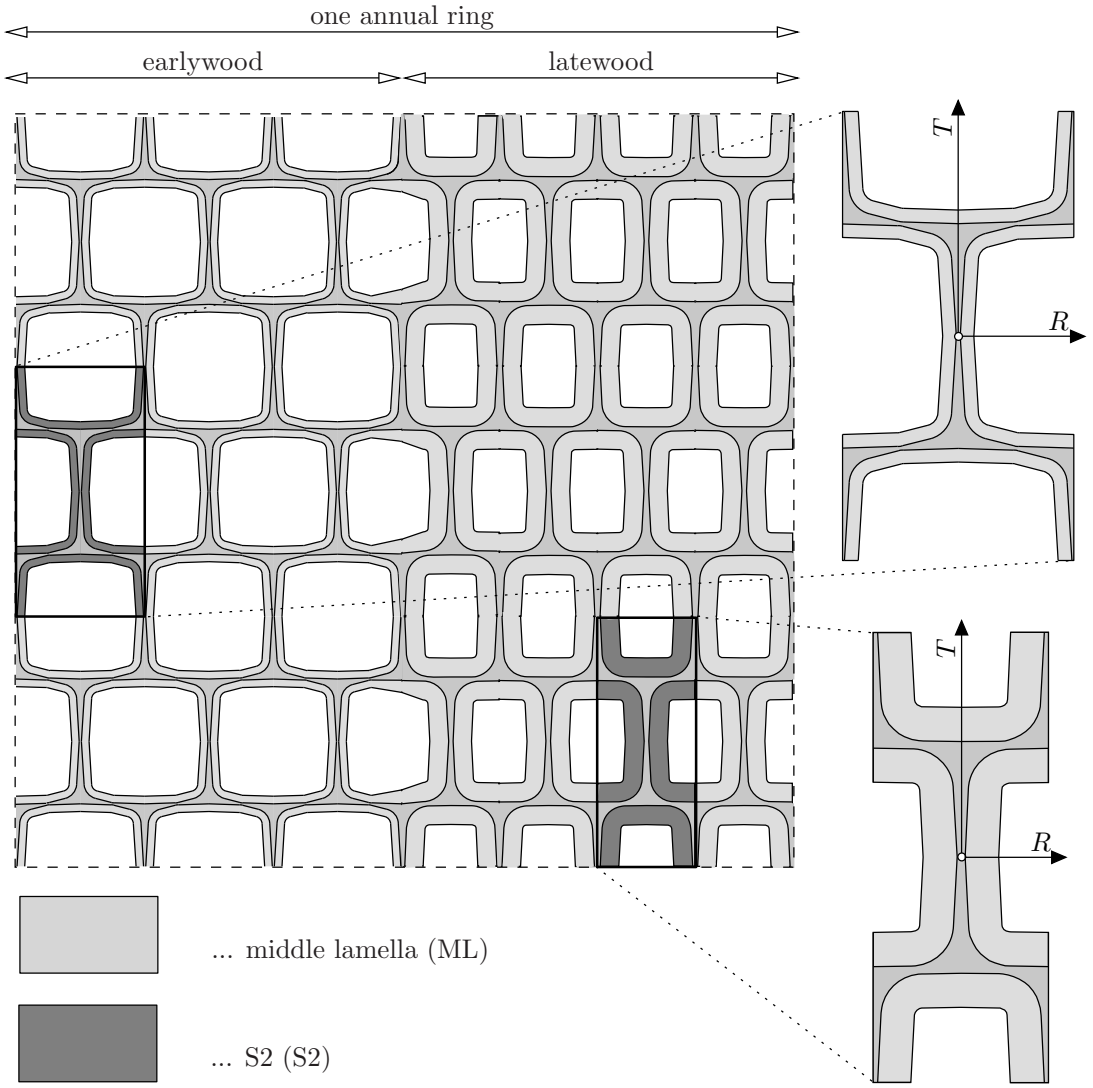

Figure 2.2: Honeycomb-like structure with extracted earlywood and latewood cell

One annual ring is built up of both an earlywood and a latewood part (see Figure 2.2). The earlywood starts to grow in the beginning of the growing season, which is from spring until fall, and latewood grows in winter. The earlywood cells are thin-walled and therefore they can be identified by their light color. In contrast, the darker part of the annual ring, the latewood, consists of cells with an opposite feature, which is a thicker wall for a better mechanical support resulting in a much higher density. For both types, earlywood and latewood cells, the tangential diameter is almost constant (about $60\,\mu m$), while the radial diameter and the total cell wall thickness varies. These wood cells are arranged in a honeycomb-like structure.

For a failure criterion to depict the crack directions within the different structures of the annual rings adequately, the annual ring must be examined on its two different cell types and on its behavior.

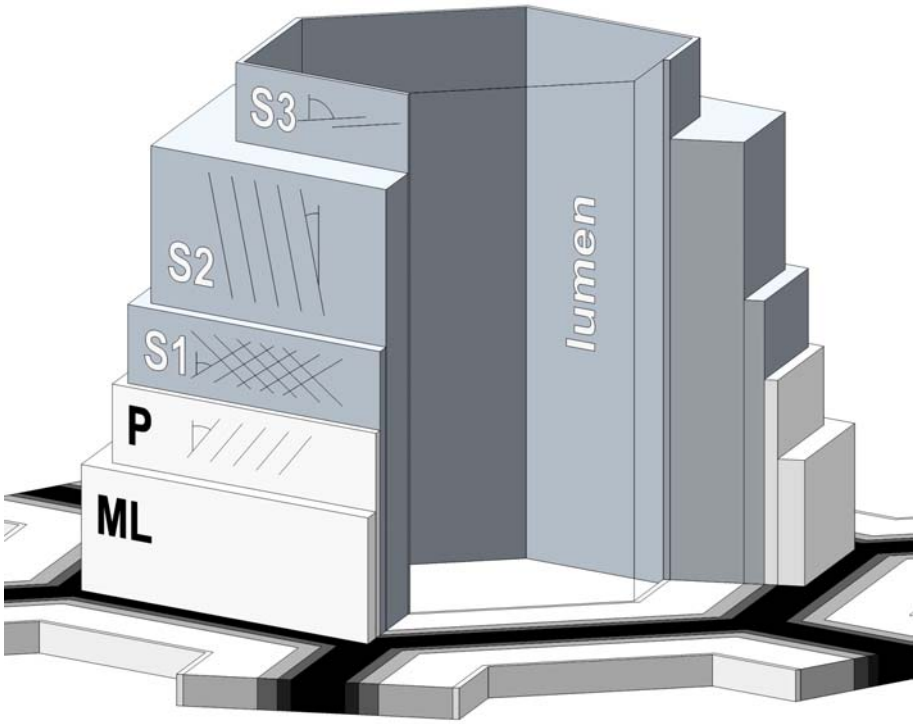

Figure 2.3: Model of the layered cell wall [8]

Such a wood cell consists of several layers, which are shown in Figure 2.3 additionally, the different micro fibril angles (MFA) of the cellulose fibers contained in their respective layer is shown in this figure. The middle lamella (*ML*) connects two neighbouring cells, the primary wall (*P*) is located between the middle lamella and the secondary wall, which is composed of the first (*S1*), second (*S2*) and third (*S3*) layer.

The thickness of a cell wall, e.g. of spruce, ranges between approximately $4\,\mu m$ for earlywood and $9.5\,\mu m$ for latewood cells. The middle lamella (*ML*) is arranged between the wood cells to hold them together and is nearly free of cellulose. The primary cell wall (*P*) is a thin layer, which is formed during cell growth by attaching cellulose microfibrils to the middle lamella. In the first layer of the secondary wall (*S1*), a high microfibril angle of the crosswisely arranged microfibrils can be observed. The second layer of the secondary wall (*S2*) is responsible for the variable cell wall thickness in earlywood ($t_{S2}^{EW} \approx 1.45 \mu m$) and latewood ($t_{S2}^{LW} \approx 4.70 \mu m$) and accounts for 80-90% of the cell wall volume [12]. With its small winding angle of the cellulose microfibrils (MFA) and the high cellulose content, it is the main supporting element in the cell wall. The third layer of the secondary wall (*S3*) is the thinnest layer of both cell walls and has microfibrils arranged with a very high microfibril angle [8].

In order to simplify the unit cell, the layers, which are assumed to have minor influence on the mechanical behavior, the layers *P*, *S1*, and *S3* haven't been modeled. For this purpose, the material characteristics of the *S2* layer were adjusted. Regarding the numerical simulation and analysis, only these two layers

(*ML* and *S2*) are modelled and considered. The reenforcing effect of the omitted layers on the *S2* layer is considered by an increase of the stiffness of this layer.

This increase of stiffness and strength and the following evaluation of the unit cell model was repeated until the crack mechanisms, after applying a specific loadcase, which are known from the examination of the macroscopic model of wood, could be observed. This two specific loadcases and the corresponding crack direction are a tensile load in R-direction leading to a tangential crack in the earlywood cell and a tensile load in T-direction leading to a radial crack through the middle lamella of the latewood cell. As a result of this parameter study, the stiffness matrix and the strength values of the *S2* layer were defined.

2.2 Unit Cell Method

To evaluate the stress states at the time of crack initiation, the unit cell method was applied. Unit cell computational homogenization methods typically include the modelling of a periodic material microstructure with repeating basic elements, the so-called unit cells. For simple microstructures, the unit cell problem can sometimes be solved analytically, yet often only a numerical solution is effective.

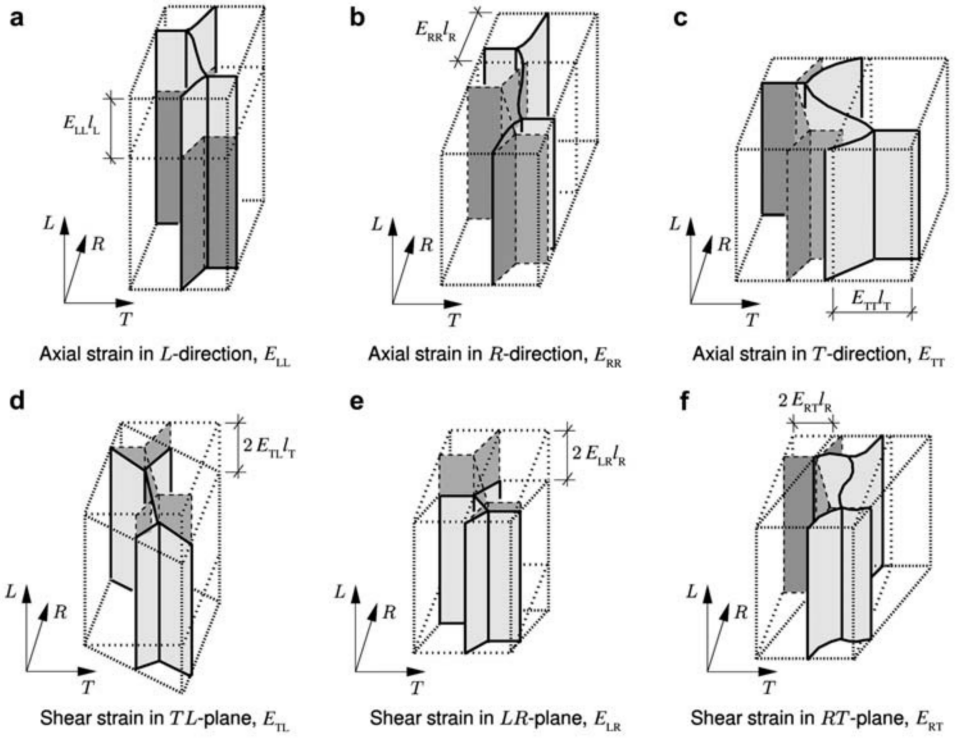

Figure 2.4: Displacement configurations related to six reference strain states E_{IJ}, $I, J = L, R, T$ [10]

The unit cell is subjected to periodic and symmetric boundary conditions for the displacements, thereby resulting macroscopic strains are linked to the spatial

average of the periodic microstresses, reading as:

$$\begin{Bmatrix} \Sigma_{RR} \\ \Sigma_{TT} \\ \Sigma_{LL} \\ \sqrt{2}\Sigma_{TL} \\ \sqrt{2}\Sigma_{LR} \\ \sqrt{2}\Sigma_{RT} \end{Bmatrix} = \begin{bmatrix} C_{RRRR} & C_{RRTT} & C_{RRLL} & 0 & 0 & 0 \\ C_{RRTT} & C_{TTTT} & C_{TTLL} & 0 & 0 & 0 \\ C_{RRLL} & C_{LLTT} & C_{LLLL} & 0 & 0 & 0 \\ 0 & 0 & 0 & 2C_{TLTL} & 0 & 0 \\ 0 & 0 & 0 & 0 & 2C_{LRLR} & 0 \\ 0 & 0 & 0 & 0 & 0 & 2C_{RTRT} \end{bmatrix} \begin{Bmatrix} E_{RR} \\ E_{TT} \\ E_{LL} \\ \sqrt{2}E_{TL} \\ \sqrt{2}E_{LR} \\ \sqrt{2}E_{RT} \end{Bmatrix}. \tag{2.1}$$

For example the macroscopic stresses as a result of a unit strain in radial direction of $E_{RR} = 1$ are

$$\begin{Bmatrix} \Sigma_{RR} \\ \Sigma_{TT} \\ \Sigma_{LL} \end{Bmatrix} = \begin{Bmatrix} C_{RRRR} \\ C_{RRTT} \\ C_{RRLL} \end{Bmatrix}, \tag{2.2}$$

with all other components of $\mathbb{C}$ being equal to zero. The remaining components of the stiffness tensor are obtained by applying additional axial strains in longitudinal and tangential directions, as well as shear strains in RT, TL and LR planes (see Figure 2.4 and [10]).

2.2.1 Geometry

Figure 2.5 shows the parameters which were used for the composition of the geometry. Based on the parameters $l_r, l_t, l_l, t_{ml}, t_{S2}, \phi$ and β_1, the geometry of the unit cell is generated automatically. All used equations for the generation of the geometry are listed in the Appendix. The automation of the geometry creation allows an easy adoption of the cell, and thus the possibility to apply this model to different clear wood densities and species.

Due to the double symmetry of the cells, the geometry generator could be simplified to a quarter piece of the cell and mirrored twice afterwards. Starting from the point of origin, all other nodes and geometry parameters can be evaluated precisely. By reference to some geometric relationships, the entire basic structure of the unit cell can ultimately be determined. This basic structure consists of the nodes shown in Figure 2.5. Since this is the unit cell of a grown material, in general, sharp transitions are rather improbable and indicate discontinuities in the structure.

As depicted in this thesis, the examination of an average and accurate case of geometry, regarding the unit cell model, is required. The remaining parameters fillet_1 and fillet_2, as fillets of edged and sharp transitions were introduced. The coordinate origin and simultaneously the node_1 (see Figure 2.5) with the two auxiliary straight lines l_1 and l_2 describe the exact position of the center axis of the unit cell. This center axis also corresponds to the plane of symmetry.

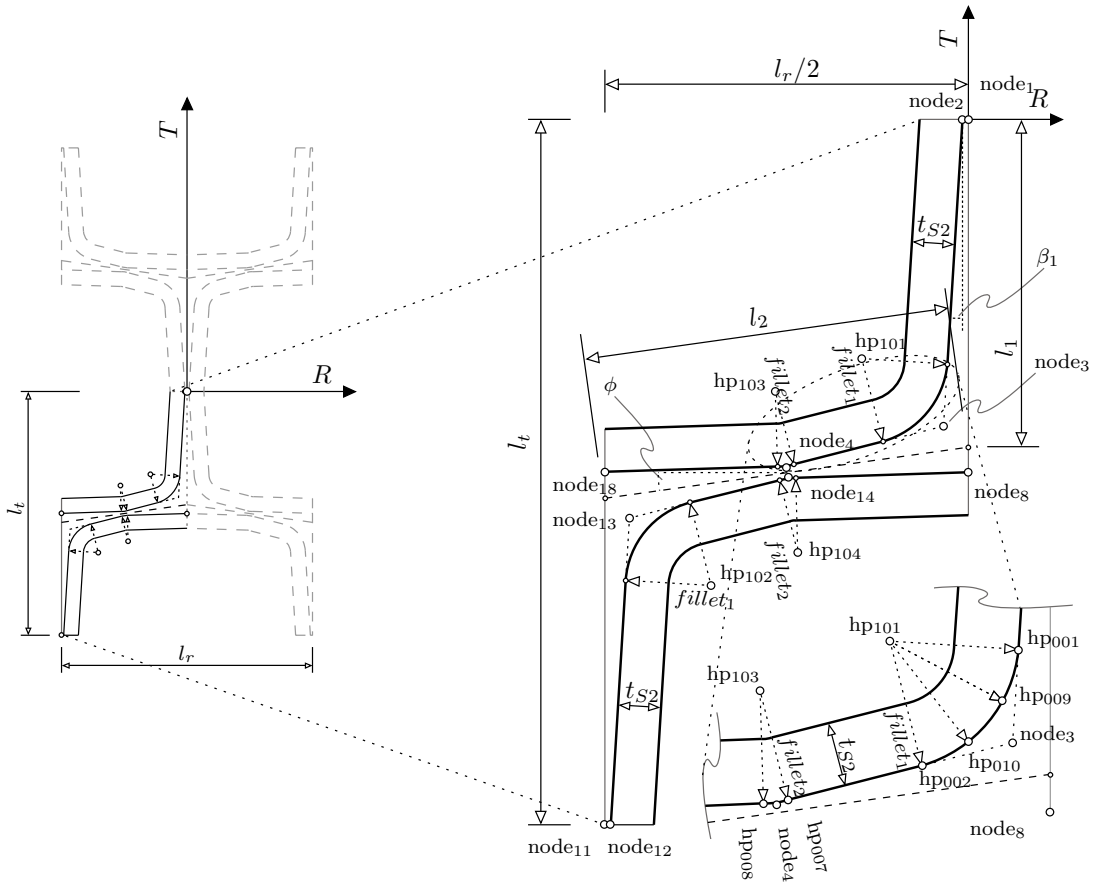

Figure 2.5: Geometry of a random unit cell, connection between input parameters and dimensions

To obtain the final geometry of the cell, the quarter section of the cell is then mirrored once along the R-axis and subsequently once along the T-axis.

For the following calculations, only two kinds of geometry of the unit cell were used. Since the main aim was to analyze the crack development, the worst possible geometry ratios had to be used. Thus, it was possible to obtain the earliest moment of crack initiation for earlywood and latewood cells, respectively.

The two main cell wall layers were examined within the framework of this thesis. These are the isotropic middle lamella and the orthotropic *S2* layer, both described briefly in the following subsections.

2.2.2 Middle Lamella

After having simplified the model of five layers to the two remaining layers *ML* and *S2* layer, merely two different materials had to be defined.

The middle lamella consists of lignin, its material properties such as elastic modulus (E), POISSON's ratio (ν) and strength (f_y) are already known by BADER [2] and could therefore be assigned directly. The material behavior of lignin has

been researched already and corresponds to a linear elastic material behavior. Based on this existing knowledge, the *ML* material has been completely defined and assigned to a single crack area, which is a partition defined in the FEM model with a single failure criterion resulting in defects, for the eXtended Finite Element method. However, as there is still considerable potential for improvement in the XFEM algorithm, which is explained more precisely in Chapter 2.2.4 and shown in Figure 2.8, more crack areas had to be used.

If a material possesses equal mechanical properties in all directions of a material, the components of the compliance matrix D_{ijkl} can not change due to a random rotation of the coordinate system. Regarding such a rotation, the components are invariant and, therefore, this material has a so-called isotropic material behavior reducing the 81 coefficients of C_{ijkl} to six equations with two independent coefficients (e.g. E and ν) of C_{ijkl}:

$$\varepsilon_{ij} = D_{ijkl}\,\sigma_{kl} \quad \text{with} \quad \mathbb{D} = \mathbb{C}^{-1}. \tag{2.3}$$

$$\begin{Bmatrix} \varepsilon_L \\ \varepsilon_R \\ \varepsilon_T \\ \gamma_{LR} \\ \gamma_{RT} \\ \gamma_{TL} \end{Bmatrix} = \begin{bmatrix} \frac{1}{E} & -\frac{\nu}{E} & -\frac{\nu}{E} & 0 & 0 & 0 \\ -\frac{\nu}{E} & \frac{1}{E} & -\frac{\nu}{E} & 0 & 0 & 0 \\ -\frac{\nu}{E} & -\frac{\nu}{E} & \frac{1}{E} & 0 & 0 & 0 \\ 0 & 0 & 0 & \frac{1}{G} & 0 & 0 \\ 0 & 0 & 0 & 0 & \frac{1}{G} & 0 \\ 0 & 0 & 0 & 0 & 0 & \frac{1}{G} \end{bmatrix} \begin{Bmatrix} \sigma_L \\ \sigma_R \\ \sigma_T \\ \tau_{LR} \\ \tau_{RT} \\ \tau_{TL} \end{Bmatrix} \tag{2.4}$$

The Drucker-Prager failure hypothesis represents an extension of the yield hypothesis of von Mises. The starting point is the formulation of von Mises' yield conditions including the so-called Coulomb friction μ. This ultimately leads to the failure criterion in (2.5) based on the failure hypothesis of Drucker-Prager:

$$f(\boldsymbol{\sigma}) \leq \sqrt{s_{ij}s_{ij}} + \frac{\mu}{\sqrt{3}} I_1^{\sigma} - \sqrt{2} f_y \tag{2.5}$$

Substituting $\mu = 0$ in (2.5) leads to a special case of this failure criterion on the basis of the yield hypothesis by von Mises. The Coulomb friction for the $S2$ layer of the used unit cell was set to $\mu = 0$, because of a lack of required experiments for a precise determination. This means that in the user subroutines the possibility of the Drucker-Prager failure criterion would exist, but the simplier criterion by von Mises was used:

$$f(\boldsymbol{\sigma}) \leq \frac{\sqrt{\sigma_{ij}\sigma_{ij}}}{\sqrt{2} f_y} \tag{2.6}$$

On basis of this hypothesis the associated yield criterion and the plastic strain tensor could be evaluated.

$$d\varepsilon_{ij}^{p} = d\lambda \left(\frac{\mu}{\sqrt{3}} \delta_{ij} + \frac{s_{ij}}{\|\mathrm{S}\|} \right) \tag{2.7}$$

By specialization of (2.7) with $\mu = 0$, the flow rule according to von Mises was obtained:

$$d\varepsilon_{ij}^{p} = de_{ij}^{p} = d\lambda \left(\frac{s_{ij}}{\|\mathrm{S}\|} \right) \tag{2.8}$$

These plastic strains were used for the calculation of the crack directions with XFEM. By the determination of the elasto-plastic strain tensor ($d\varepsilon_{ij}^{p}$), which is a function of the stress tensor (s_{ij}), the main distortion direction and thereby the maximum of the principal strains on its perpendicular cracking plane can be defined.

This theoretical background for the von Mises failure criterion leads to the only definition for an applied failure criterion for the middle lamella which was used for the evaluation of all unit cells. Additionally, the crack direction was determined on the basis of the maximum principal strain at the point of failure which is perpendicular to the cracking plane.

The following parameters for stiffness and strength were used for the linear elastic isotropic material for the middle lamella, see (2.9) for stiffness and (2.10) for strength values.

$$E = 5927.7 \text{ MPa} \qquad \nu = 0.3157 \tag{2.9}$$

$$f_y = 14.3 \text{ MPa} \tag{2.10}$$

This calculation of stresses and plastic strains for both materials used in this FE model is shown in the *Abaqus™* user subroutine input file (see Listing 2.1). A user damage initiation subroutine for *Abaqus™* is used to determine the moment of crack initiation and the related crack plane of each FEM element. More precisely, the stress tensor $\boldsymbol{\sigma}$, the tensor of plastic strains $\boldsymbol{\varepsilon}^{p}$ and the related normal vector of the crack plane are defined for each element and therefore the failure criterion is determined.

Within this user subroutine (see Listing 2.1), two different failure criteria, one criterion for each of the two used materials, were defined. For the material of the middle lamella the von Mises failure criterion was used, which consists one parameter (f_y). If the threshold for the failure criterion ($f(\boldsymbol{\sigma}) = 1$) is reached or exceeded, crack initiation starts and, hence, the direction of the corresponding crack plane has to be determined.

To calculate this direction the strain tensor $\boldsymbol{\varepsilon}^{p}$ gets defined by means of Equation (2.8) and the main strain direction is calculated afterwards, which defines the normal vector and has to be perpendicular to the crack plane.

2.2.3 S2 Layer

This layer is a fiber-matrix composite consisting of lignin and cellulose fibers. The fibers are oriented in longitudinal direction of the timber cell, yet there is also a spatial rotation of the fibers about the micro fibril angle (MFA). This angle is a further input parameter for the modelling of the unit cell and may therefore be varied. It influences the local orientation of the *S2* partitions (see Figure 2.8).

As already mentioned, some simplifications have been made. One of the major simplifications was to neglect the cell wall layers *P*, *S1* and *S3*. The loss of stiffness and strength could be compensated by increasing the *S2* material parameters. Due to the lack of experiments and measurement data, no accurate correction values of the *S2* parameters could be used.

As some crack modes of timber are known by means of the macromechanical model and therefore also the corresponding strengths are relatively precisely determined, the stiffness and strength of the *S2* layer were gradually increased until the desired crack mode and the corresponding failure strength became apparent. In this process the parametric study was applied. One of these crack modes is the delamination of the cell walls. This corresponds to a radial crack through the middle lamella, which has to appear first at the latewood cell once tangential load was applied.

The second crack mode examined, a complete rupture of the cell walls, regards the earlywood cell and occurs in the tangential direction due to a radial load. The correction values obtained for the stiffness matrix and the strength of the *S2* layer amounts to a factor of approximately three. The rather high increase of stiffness and strength values, can be explained by the *P*, *S1* and *S3* layer acting as a protective cover for the *S2* layer.

The mechanical behavior of wood regarding plasticity can be described by the orthotropic failure criterion of Tsai and Wu [22], which was proven by Eberhardsteiner [6] to appropriately describe the onset of "plastic behavior" of wood. Its mathematical description reads as

$$a_{ij}\sigma_{ij} + b_{ijkl}\sigma_{ij}\sigma_{kl} + c_{ijklmn}\sigma_{ij}\sigma_{kl} + ... = 1 \ , \qquad i,j,k,l,m,n = L,R,T \quad (2.11)$$

where a_{ij}, b_{ijkl} and c_{ijklmn} are material related components of tensors of second, forth and sixth order. When restricted to a formulation of second order and considering symmetry of the tensor coefficients:

$$a_{ij} = a_{ji}, b_{ijkl} = b_{jikl} = b_{klij} (= b_{jilk}, b_{ijlk}) \quad (2.12)$$

the number of independent components for orthotropic materials reduces from six to three for a_{ij} and from 21 to nine for b_{ijkl}, respectively, which yields

$$\mathbf{a} = \begin{Bmatrix} a_{LL} \\ a_{RR} \\ a_{TT} \end{Bmatrix}, \mathbf{b} = \begin{bmatrix} b_{LLLL} & b_{LLRR} & b_{LLTT} & 0 & 0 & 0 \\ & b_{RRRR} & b_{RRTT} & 0 & 0 & 0 \\ & & b_{TTTT} & 0 & 0 & 0 \\ & & & b_{RTRT} & 0 & 0 \\ & \text{sym.} & & & b_{LTLT} & 0 \\ & & & & & b_{LRLR} \end{bmatrix} \quad (2.13)$$

The failure criterion of Tsai and Wu [22] for orthotropic materials with different strengths in tension and compression is used to define local failure, reading:

$$\begin{aligned} f(\boldsymbol{\sigma}) = a_{LL}\sigma_{LL} + a_{RR}\sigma_{RR} + a_{TT}\sigma_{TT} + \\ b_{LL}\sigma_{LL}^2 + b_{RR}\sigma_{RR}^2 + b_{TT}\sigma_{TT}^2 + \\ 2b_{LLRR}\sigma_{LL}\sigma_{RR} + 2b_{RRTT}\sigma_{RR}\sigma_{TT} + 2b_{TTLL}\sigma_{TT}\sigma_{LL} + \\ 4b_{LRLR}\tau_{LR}^2 + 4b_{RTRT}\tau_{RT}^2 + 4b_{TLTL}\tau_{TL}^2 \leq 1 \end{aligned} \tag{2.14}$$

The components in (2.14) are described in terms of tension, compression and shear strength properties of the material.

As this material consists of a composite material of fiber embedded in a matrix, a failure criterion specialized for these kinds of materials developed by Puck [19] was used. Three different combinations of the components of $\boldsymbol{\sigma}$ were used to define the failure mechanisms of the *S2* layer:

$$f_1(\boldsymbol{\sigma}) \leq \frac{\sigma_{LL,rot}}{f_{t,L,rot}} \tag{2.15}$$

$$f_2(\boldsymbol{\sigma}) \leq \frac{\sigma_{TT,rot}}{f_{t,T,rot}} \tag{2.16}$$

$$f_3(\boldsymbol{\sigma}) \leq \left(\frac{\sigma_{RT,rot}}{f_{v,RT,rot}}\right)^2 + \left(\frac{\sigma_{TL,rot}}{f_{v,TL,rot}}\right)^2 \tag{2.17}$$

The stiffness matrix, which was used for the reinforced *S2* layer, is represented in Equation (2.18). It has to be pointed out that the material behavior of the *S2* layer is transversal isotropic because $C_{1111} = C_{2222}$ holds. The stiffness matrix is rotated by the MFA out of the global coordinate system from the global L-direction into the direction of the micro fibrils whereby the R-direction is perpendicular to the cell wall. Therefore, strength values, stress components and stiffness matrix are labelled by an additional index "rot", denoting a rotation of the local coordinate system, as discribed above. For both remaining directions (R and T-direction), the material behavior related to their stiffness is identical.

$$\mathbb{C}_{rot} = \begin{bmatrix} C_{1111} & C_{1122} & C_{1133} & C_{1123} & C_{1113} & C_{1112} \\ & C_{2222} & C_{2233} & C_{2223} & C_{2213} & C_{2212} \\ & & C_{3333} & C_{3323} & C_{3313} & C_{3312} \\ & & & C_{2323} & C_{2313} & C_{2312} \\ & \text{sym.} & & & C_{1313} & C_{1312} \\ & & & & & C_{1212} \end{bmatrix}$$
$$= \begin{bmatrix} 38212 & 20744 & 14632 & & & \\ & 38212 & 14632 & & & \\ & & 230344 & & & \\ & & & 8732 & & \\ & \text{sym.} & & & 7908 & \\ & & & & & 7908 \end{bmatrix} \text{[MPa]} \tag{2.18}$$

Following strength values (2.19) were used for the evaluation of the failure criteria explained above:

$$\begin{aligned} f_{t,L,rot} &= 175 \text{ MPa}, & f_{t,T,rot} &= 60 \text{ MPa}, \\ f_{v,RT,rot} &= 45 \text{ MPa}, & f_{v,TL,rot} &= 35 \text{ MPa}. \end{aligned} \tag{2.19}$$

Using this knowledge of three different failure mechanisms and their definition of the related stress tensor $\boldsymbol{\sigma}$ of the *S2* layer, a distinction of these three failure mechanisms is done and thereby the according crack plane.

This definition of the moment of the crack initiation and the related normal vector which defines the direction of the cracking plain, is explained hereafter (see Listing 2.1).

On the basis of equations (2.15), (2.16) and (2.17), it is obvious that the normal vector, which defines the direction of the cracking plane, is in L-direction of the local coordinate system for the failure mechanism $f_1(\boldsymbol{\sigma})$. The normal vector of the cracking plane for the failure mechanisms $f_2(\boldsymbol{\sigma})$ and $f_3(\boldsymbol{\sigma})$ points into T-direction of the local datum of each *S2* layer partition. This means the failure mechanisms $f_2(\boldsymbol{\sigma})$ and $f_3(\boldsymbol{\sigma})$ will always lead to a cracking plane being perpendicular to the cell wall orientation, only differing in the direction in which the crack opens, perpendicular or parallel to the cracking plane.

Listing 2.1: Users value for damage initiation, udmgini.f

```
1        INCLUDE 'uvarm.f'
2        SUBROUTINE UDMGINI(FINDEX,NFINDEX,FNORMAL,NDI,NSHR,NTENS,
             PROPS,
3       1 NPROPS,STATEV,NSTATEV,STRESS,STRAIN,STRAINEE,LXFEM,TIME,
4       2 DTIME,TEMP,DTEMP,PREDEF,DPRED,NFIELD,COORDS,NOEL,NPT,
5       3 KLAYER,KSPT,KSTEP,INC,KDIRCYC,KCYCLELCF,TIMECYC,SSE,SPD,
6       4 SCD,SVD,SMD,JMAC,JMATYP,MATLAYO,LACCFLA,CELENT,DROT,ORI)
7        INCLUDE 'ABA_PARAM.INC'
8  !
9  !c DEFINITIONS AND DIMENSIONS
10 !
```

```
11        DIMENSION FINDEX(NFINDEX),FNORMAL(NDI,NFINDEX),COORDS(*),
12       1 STRESS(NTENS),STRAIN(NTENS),STRAINEE(NTENS),PROPS(NPROPS),
13       2 STATEV(NSTATEV),PREDEF(NFIELD),DPRED(NFIELD),TIME(2),
14       3 JMAC(*),JMATYP(*),DROR(3,3),ORI(3,3)
15  !
16        REAL*8 MULT(3), S(6), PS(3), AN(3,3), CPlane(3,3), Eps(6),
             NPlane(3), ANPlane(3,3), s_abs
17  !
18  ! DESTINCTION BETWEEN MATERIALS (ML AND S2)
19  !
20        IF (PROPS(3) .eq. 0.0d0) THEN
21  !
22  ! CALCULATE STRESS INVARIANTS SINV1 AND SINV2
23  !
24          CALL SINV(STRESS,SINV1,SINV2,NDI,NSHR)
25  !
26  ! CALCULATE PRINCIPAL STRESS VALUES AND DIRECTIONS
27  !
28          CALL SPRIND(STRESS,PS,AN,1,NDI,NSHR)
29          S(1) = STRESS(1)
30          S(2) = STRESS(2)
31          S(3) = STRESS(3)
32          S(4) = STRESS(4)
33          S(5) = STRESS(5)
34          S(6) = STRESS(6)
35  !
36  ! DRUCKER - PRAGER FAILURE CRITERION / VON MISES FAILURE
       CRITERION
37  !
38          r=dsqrt((1d0/3d0)*((S(1)-S(2))**2+(S(2)-S(3))**2+(S(3)-S
               (1))**2+6*(S(4)**2+S(5)**2+S(6)**2)))
39          FINDEX(1) = (r + PROPS(2)/(dsqrt(3d0))*SINV1)/(dsqrt(2d0)
               *PROPS(1))
40  !
41  ! CALCULATION OF STRAIN TENSOR AND PRINCIPAL STRAINS
42  !
43          Eps(1) = PROPS(2)/dsqrt(3d0)+S(1)/r
44          Eps(2) = PROPS(2)/dsqrt(3d0)+S(2)/r
45          Eps(3) = PROPS(2)/dsqrt(3d0)+S(3)/r
46          Eps(4) = S(4)/r
47          Eps(5) = S(5)/r
48          Eps(6) = S(6)/r
49  !
50          CALL SPRIND(Eps,NPlane,ANPlane,2,NDI,NSHR)
51  !
52  ! MAXIMUM PRINCIPAL STRAIN FOR CRACK PLANE DIRECTION
53  !
54          SIG1 = NPlane(1)
55          KMAX=1
56          DO K1 = 2, NDI
57            IF(NPlane(K1).GT.SIG1) THEN
58              SIG1 = NPlane(K1)
59              KMAX = K1
60            END IF
```

```
61          END DO
62  !
63          DO K1=1, NDI
64            FNORMAL(K1,1) = ANPlane(KMAX,K1)
65          END DO
66  !
67        ELSE
68  !
69  ! MAXIMUM PRINCIPAL STRESS CRITERION FOR S2 LAYER
70  !
71          S(1) = STRESS(1)
72          S(2) = STRESS(2)
73          S(3) = STRESS(3)
74          FINDEX(1)=S(3)/PROPS(1)
75  !
76          DO K1=1, NDI
77            FNORMAL(K1,1)=ORI(K1,3)
78          END DO
79          FINDEX(2)=(S(2)/PROPS(2))
80  !
81          DO K1=1, NDI
82            FNORMAL(K1,2)=ORI(K1,2)
83          END DO
84          FINDEX(3)=(S(4)/PROPS(3))**2.0+(S(6)/PROPS(3))**2.0
85  !
86          DO K1=1, NDI
87            FNORMAL(K1,3)=ORI(K1,2)
88          END DO
89        END IF
90  !
91        RETURN
92        END
```

2.2.4 Principle of Modelling

Further, the mesh fineness and mesh structure have to be pointed out. Since the external dimensions of the unit cell amount to approximately $50 - 100\,\mu m$, the edge length of the elements is defined to 0.2 μm. Linear, reduced continuum elements (C3D8R), i.e. elements with 8 nodes and 6 element surfaces, were used. This leads to a sufficiently accurate mesh fineness regarding the transitions as well as the fillets. This leads to a mesh fineness of two elements in the direction of the smallest unit cell dimension, the longitudinal direction.

Figure 2.6 shows an FE model of an earlywood unit cell with its mesh fineness. The same is illustrated in Figure 2.7 for a latewood cell.

Considering that the XFEM code is a relatively new development, there are some shortcomings to reveal. One of these concerns is the lack of a possibility to perform a second transection once the element has already been cracked. Another limitation concerns the inability of XFEM to open several cracks in a crack domain, albeit this can in fact be explained logically in terms of the initial crack

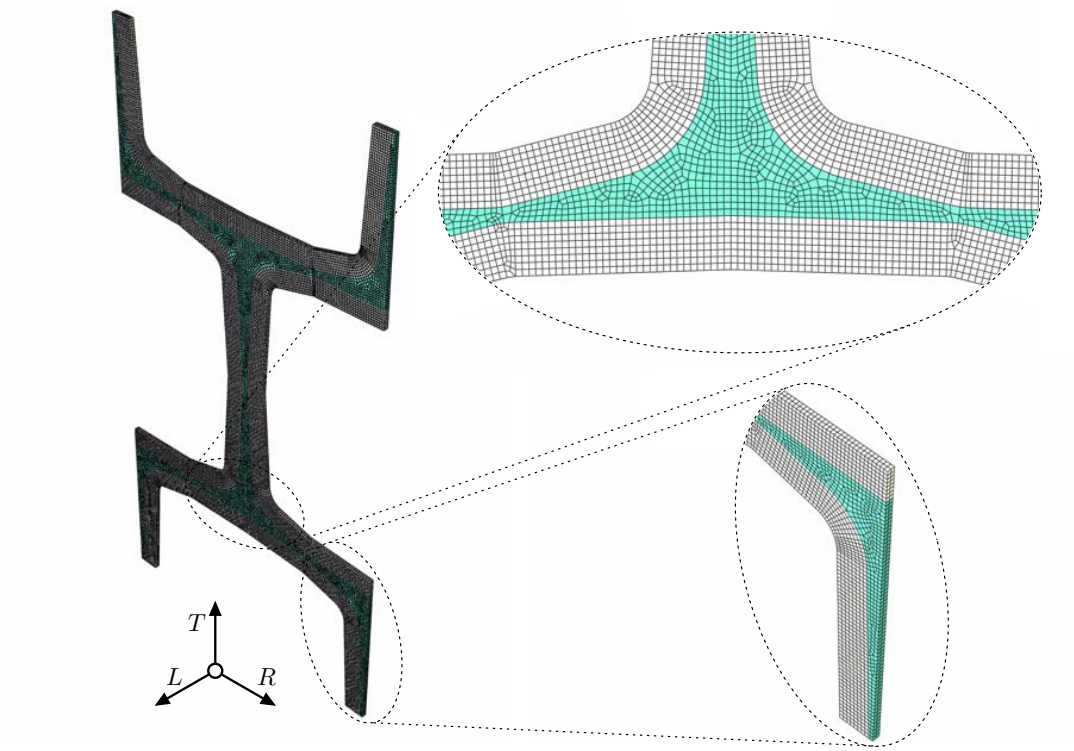

Figure 2.6: Meshing of an Earlywood Unit Cell

that occurs in the crack domain. This initial crack would spread subsequently around the initial crack due to stress redistribution and stress concentrations.

In the unit cell analysis, however, this aspect was very cumbersome since two cracks in one single element led to an uncontrolled termination of *Abaqus™*. In particular for the analysis of the unit cell with periodic boundary conditions, which resulted in the crack formation in several locations, some numerical settings had to be adjusted. Therefore, some assumptions had to be made which were able to counteract this occurrence of software deficiencies. The increment steps were set to a minimum, which reduced the crash frequency. Despite this improvement, they didn't enable the software to allow multiple initial cracks. The introduction of multiple domains extended the model to a point that in each domain a crack could now arise. Figure 2.8 shows the definition of the different crack domains. In the *S2* layer not only new crack domains were defined, the local coordinate system was rotated as well due to the microfibril angle of the cellulose fibers. As with the partitions of the *S2* layer, the crack mode of the cells' delamination could not be displayed, even in the homogeneous middle lamella additional cracking domains had to be introduced. Due to this extension, the numerical model was finally enabled to start with two cracks that ultimately connect and subsequently should lead to transecting the entire cell.

A possible alternative to the partitions with own crack domains would be the deliberate incorporation of discontinuities to the cell structure or a connecting

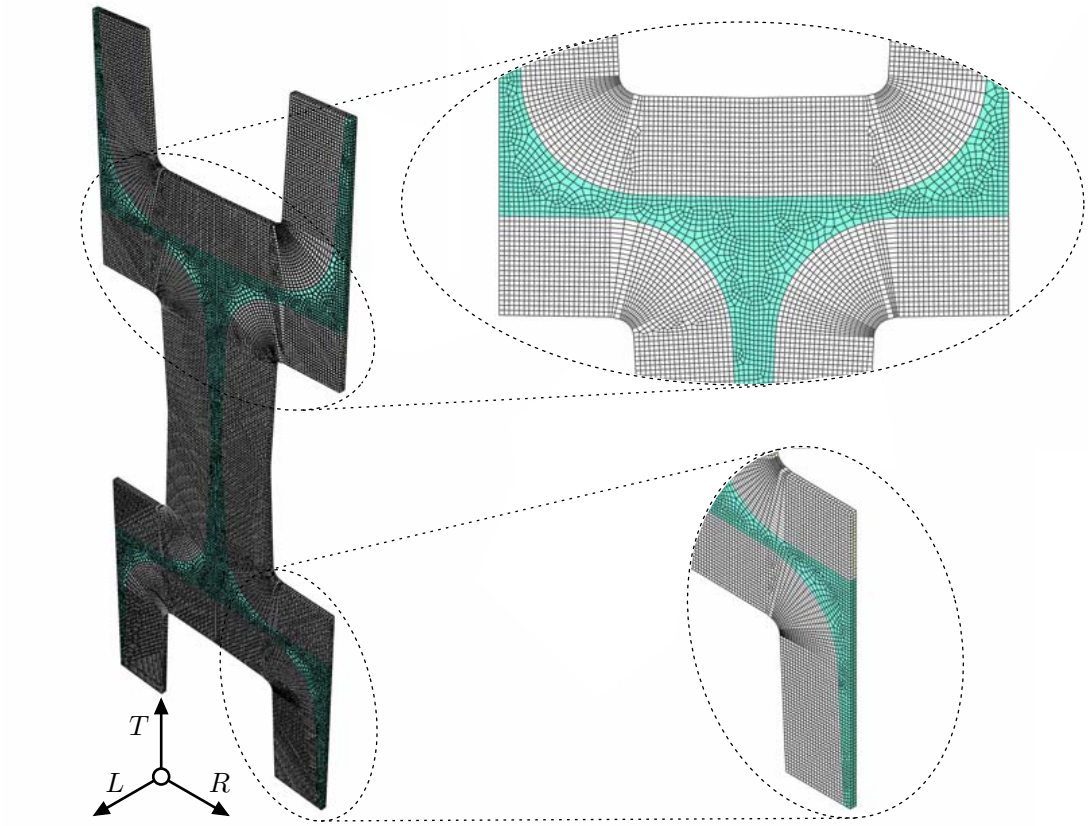

Figure 2.7: Meshing of a Latewood Unit Cell

cohesive layer between the *ML* and the *S2* layer. By introducing discontinuities, however, the exact position of the initial crack would be given, hence this version has been waived. Nor could the cohesive layer depict the desired failure modes and the corresponding failure strengths, hence they were not further analysed.

For the discrete crack modelling and crack analysis, a definition of the crack region is essential. By using the XFEM code, the so-called conventional elements are accumulated with an additional integration point. When achieving or exceeding the failure strength, it is therefore possible for XFEM to incorporate a crack and the corresponding crack plane in the respective element and, subsequently, to transect this element.

Figure 2.9 illustrates the characteristic stress-strain behavior of a material undergoing damage. The solid curve in the figure represents the damaged stress-strain response, while the dashed curve is the response in the absence of damage. As discussed later, the damaged response depends on the element dimensions such that mesh dependency of the results is minimized.

In Figure 2.9 σ_{y0} and $\bar{\varepsilon}_0^{el}$ are the yield stress and equivalent elastic strain at the onset of damage, and $\bar{\varepsilon}_f^{pl}$ is the equivalent plastic strain at failure. That is,

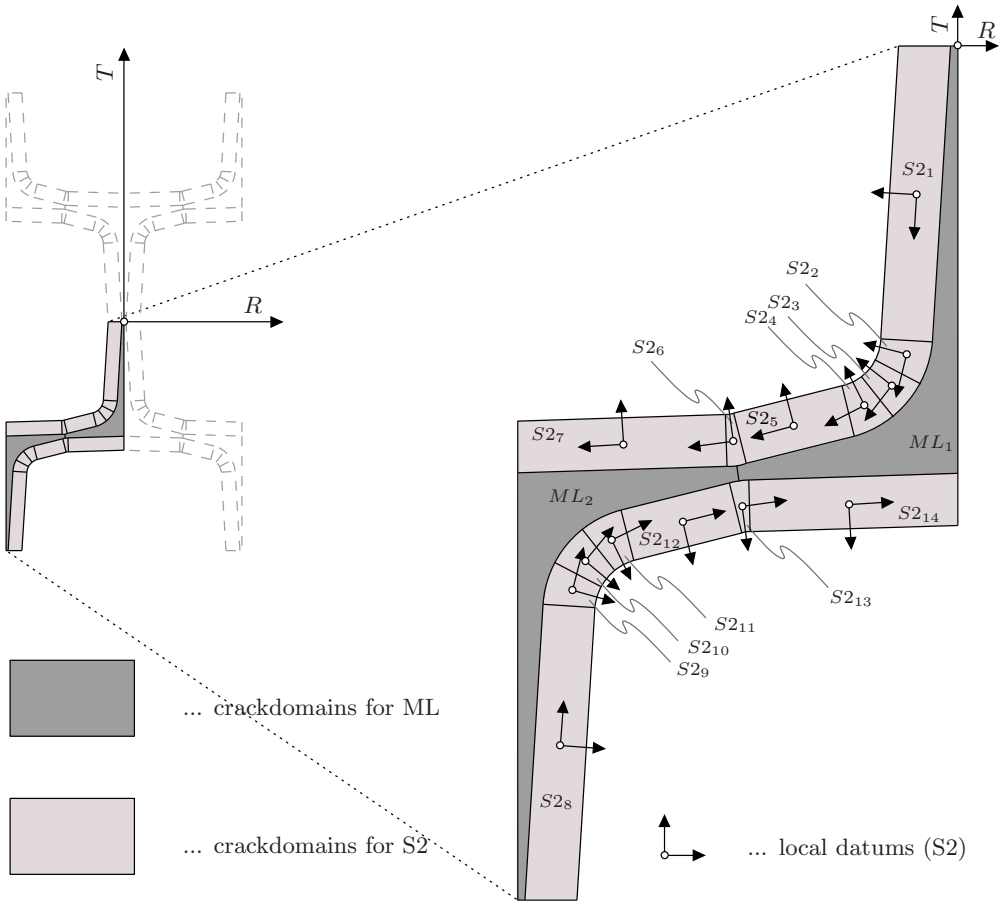

Figure 2.8: Crack Domains and local datums

when the overall damage variable reaches the value $d = 1$.

The value of the equivalent plastic strain at failure, $\bar{\varepsilon}_f^{pl}$, depends on the characteristic length of the element and cannot be used as a material parameter.

When material damage occurs, the stress-strain relationship no longer accurately represents the material's behavior. Continuing to use the stress-strain relation introduces a strong mesh dependency based on strain localization, such that the energy dissipated decreases as the mesh is refined.

The implementation of this stress-displacement concept in an FE model requires the definition of a characteristic length (l_{char}) associated with an integration point.

Equation (2.20) depicts the plastic displacement before damage initiation and equation (2.21) shows the plastic displacement after damage initiation.

$$\dot{\bar{u}}^{pl} = 0 \tag{2.20}$$

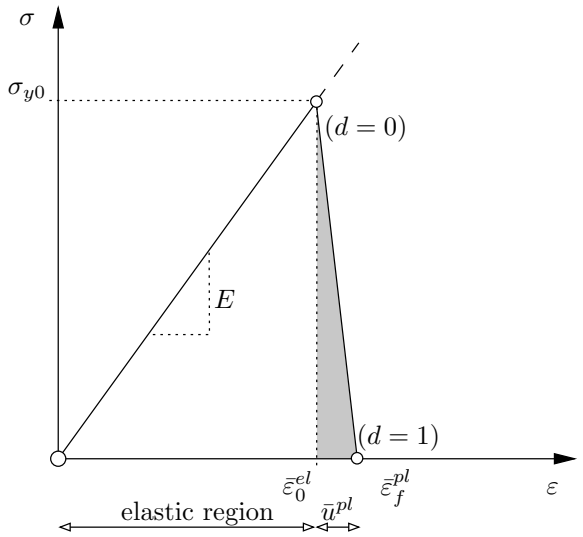

Figure 2.9: Stress-strain curve with progressive damage degradation

$$\dot{\bar{u}}^{pl} = l_{char}\dot{\bar{\varepsilon}}^{pl} \tag{2.21}$$

The definition of the characteristic length depends on the element geometry and formulation. It is a typical length of a line across an element for a first-order element and it is half of the same typical length for a second-order element. This definition of the characteristic length is used because the direction in which the fracture occurs is not known in advance. Therefore, elements with large aspect ratios will have rather different behavior depending on the direction in which they crack. Some mesh sensitivity remains because of this effect, and elements that have aspect ratios close to unity are recommended.

As discussed previously, once the damage initiation criterion has been reached, the effective plastic displacement ($\bar{u}^{pl}$) is defined with the evolution equation (2.21), whereby l_{char} is the characteristic length of the element.

The evolution of the damage variable with the relative plastic displacement was specified in linear form. Instantaneous failure will occur if the plastic displacement at failure ($\bar{u}_f^{pl}$) is specified as 0. In this calculation model a plastic displacement at failure of $\bar{u}_f^{pl} = 0.0001$ for the middle lamella and $\bar{u}_f^{pl} = 0.00001$ for the *S2* layer was used, causing a brittle material behavior.

Assuming a linear evolution of the damage variable with effective plastic displacement, as shown in Figure 2.10, one can specify the effective plastic displacement ($\bar{u}_f^{pl}$) at the point of failure (full degradation). Then, the damage variable increases according to

$$\dot{d} = \frac{l_{char}\dot{\bar{\varepsilon}}^{pl}}{\bar{u}_f^{pl}} = \frac{\dot{\bar{u}}^{pl}}{\bar{u}_f^{pl}} \tag{2.22}$$

This definition ensures that when the effective plastic displacement reaches

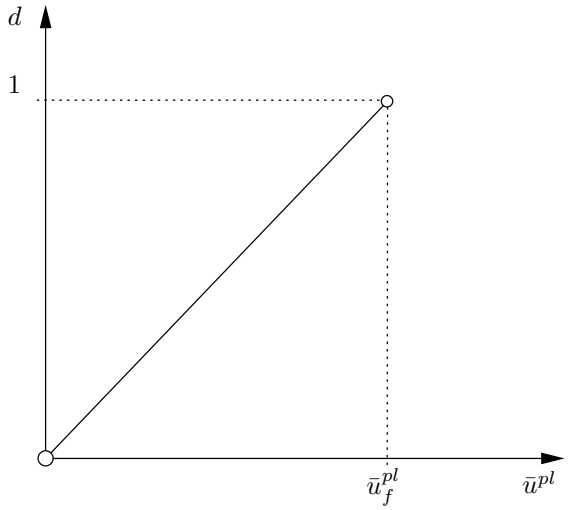

Figure 2.10: Definition of damage evolution based on a linear plastic displacement [1]

the value $\bar{u}^{pl} = \bar{u}_f^{pl}$, the material stiffness will be fully degraded ($d = 1$). The linear damage evolution law defines a truly linear stress-strain softening response only if the effective response of the material is perfectly plastic (constant yield stress) after damage initiation. [1]

2.3 Periodic Boundary Conditions

As already mentioned, for the definition of boundary conditions so-called *periodic boundary conditions* were used. By using these formulations, it is possible to define the load and the behavior as if the cell consisted of an infinite number of cells, lined up in all directions of the coordinate system. Loading is applied through prescribed displacements and is formulated by the use of the periodic boundary conditions on the basis of the so-called master node. Figure 2.11 illustrates at which point such a unit cell was extracted from its cell construct and how the master nodes were designated for the use of the periodic boundary conditions.

In such a case the boundaries have to appear in parallel pairs of corresponding surfaces denoted as k^+ and k^-, and for which applies:

$$^{k^+}\mathbf{u}(\mathbf{x}) - ^{k^-}\mathbf{u}(\mathbf{x}) =^0 \varepsilon \Delta^k \mathbf{x} \qquad \forall \mathbf{x} \epsilon^k \Gamma \tag{2.23}$$

where $\Delta^k \mathbf{x}$ is a constant distance vector between the corresponding surfaces. This boundary conditions are directly applied as multi point constraints in the case of the used displacement based FEM solver. [18]

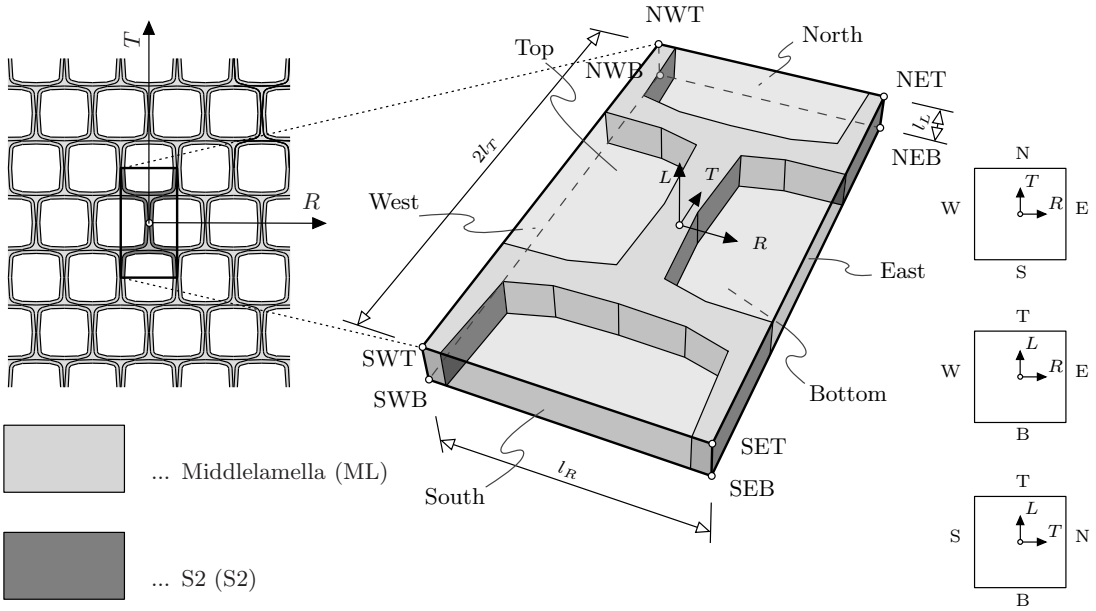

Figure 2.11: Periodic boundary condition with its master nodes

Chapter 3

Results

Based on the previously presented FEM models, cracking of early- and latewood cells was investigated. As not every geometry of a timber cell could be considered to determine crack areas, the worst case scenario was selected. It is assumed that a crack in wood has its origin at its weakest point or at a defect. Since we used FEM models without defects which would lead to an ideal macro-mechanical condition under periodic boundary conditions, the geometry with the worst possible dimensions had to be used in order to get the best approximation of the reality.

3.1 Loadcases

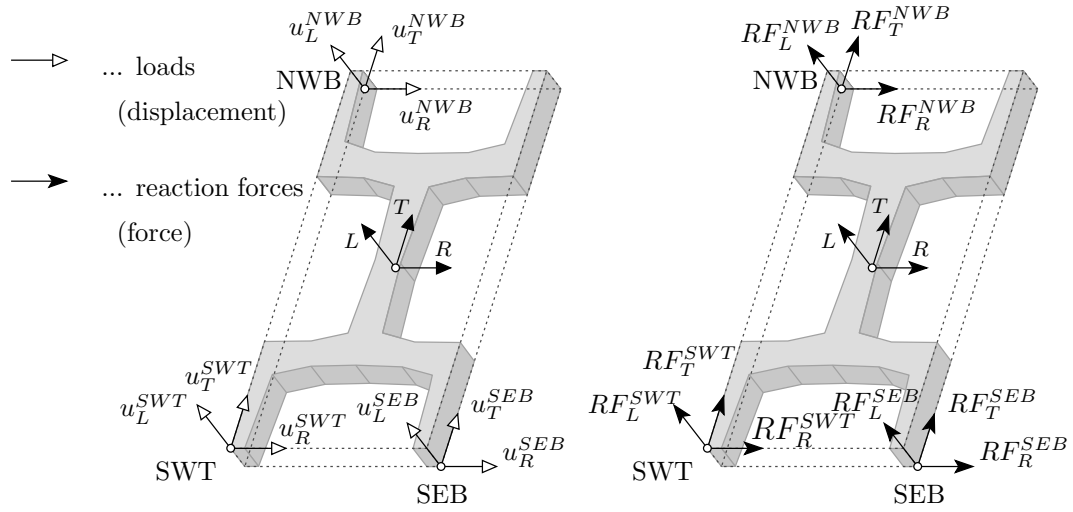

Figure 3.1: Applied loadcases and resulting reaction forces at master nodes for EW cells

Figure 3.1 and Figure 3.2 show the arrangement of the applied displacements and the resulting reaction forces distinguished in earlywood and latewood cells.

For this model, displacement-controlled loads were applied, i.e. the so-called master nodes have been shifted in R, T or L-direction. This resulted in tension and/or shear which initially had a small elastic component and ultimately led to the occurrence of failure.

By means of the occurring reaction forces on the three master nodes and the corresponding unit cell's cut surface, a stress tensor for each analyzed load case was determined over time.

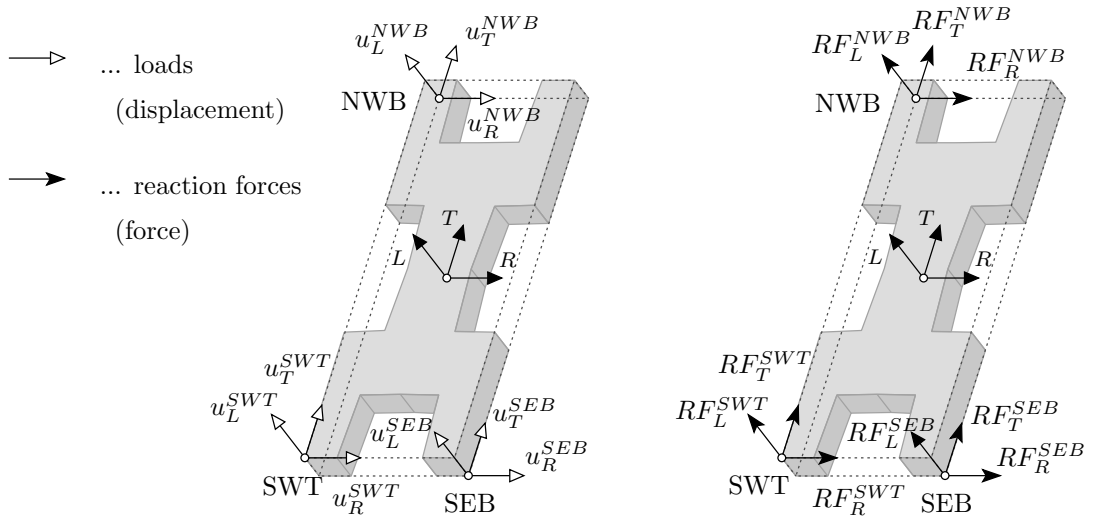

Figure 3.2: Applied loadcases and resulting reaction forces at master nodes for LW cells

An applied displacement u_R^{SEB} at its corresponding master node *SEB* results in a tensile load in R-direction, equally an applied displacement u_T^{NWB} at its corresponding master node *NWB* leads to a tensile load in T-direction of the unit cell.

For the determination of the unit cells' stress tensor all reaction forces RF had to be taken into account.

$$\boldsymbol{\sigma_{hom}} = \frac{1}{2 \cdot V} \cdot \left(\boldsymbol{RF^{-1}} \cdot \boldsymbol{P} + \boldsymbol{P^{-1}} \cdot \boldsymbol{RF} \right), \tag{3.1}$$

in

$$\boldsymbol{RF} = \begin{bmatrix} RF_R^{SEB} & RF_T^{SEB} & RF_L^{SEB} \\ RF_R^{NWB} & RF_T^{NWB} & RF_L^{NWB} \\ RF_R^{SWT} & RF_T^{SWT} & RF_L^{SWT} \end{bmatrix}, \boldsymbol{P} = \begin{bmatrix} l_R & 0 & 0 \\ 0 & 2l_T & 0 \\ 0 & 0 & l_L \end{bmatrix} \text{ and } V = l_R \cdot 2l_T \cdot l_L. \tag{3.2}$$

For a complete determination of the failure criterion the load combinations in L-direction would have had to be consulted additionally.

As this thesis shall provide a proof of concept for the determination of an entire failure criterion of wood, which means a distinction between earlywood

and latewood cells and their different cracking behavior, it was not possible to consider every loadcase.

Considering just the RT-plane, as loads yield only principal stresses in R, T and L-directions and associated shear loads in the RT-plane, not every stress component of the examined unit cell can be derived.

To prove correctness of this procedure, some load combinations in L-direction will be calculated and interpreted in the following. These examples should serve as reference, illustrating how the entire stress area may be derived in future works, including associated failure criterion and crack direction.

3.2 Results and Verification

All load cases for earlywood and latewood were determined separately, as both cell structures lead to a distinct and therefore different failure criterion.

As not merely the crack initiation was given as an objective of these failure criteria, the crack directions had to be identified as well.

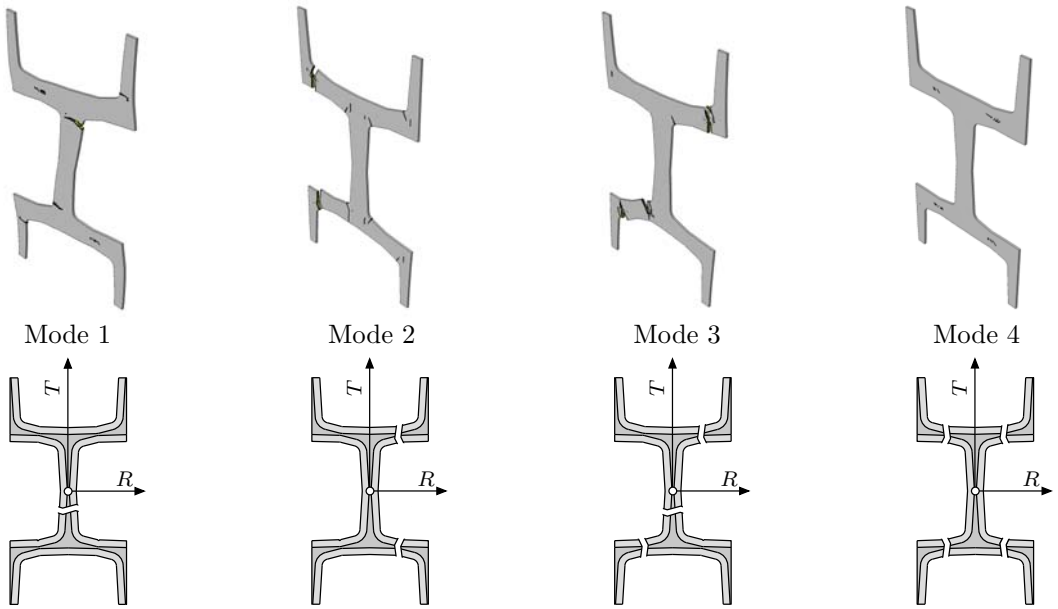

Figure 3.3: Distinction of four crack modes of an EW unit cell

Figures 3.3 and 3.4 illustrate the four defined crack directions and crack modes for the unit cells, respectively.

To obtain a summary of all crack initiations and crack modes for each evaluated loadcase, the timestep at the transition from elastic to non-linear behavior, the timestep at the point of failure as well as the crack mode were collected manually.

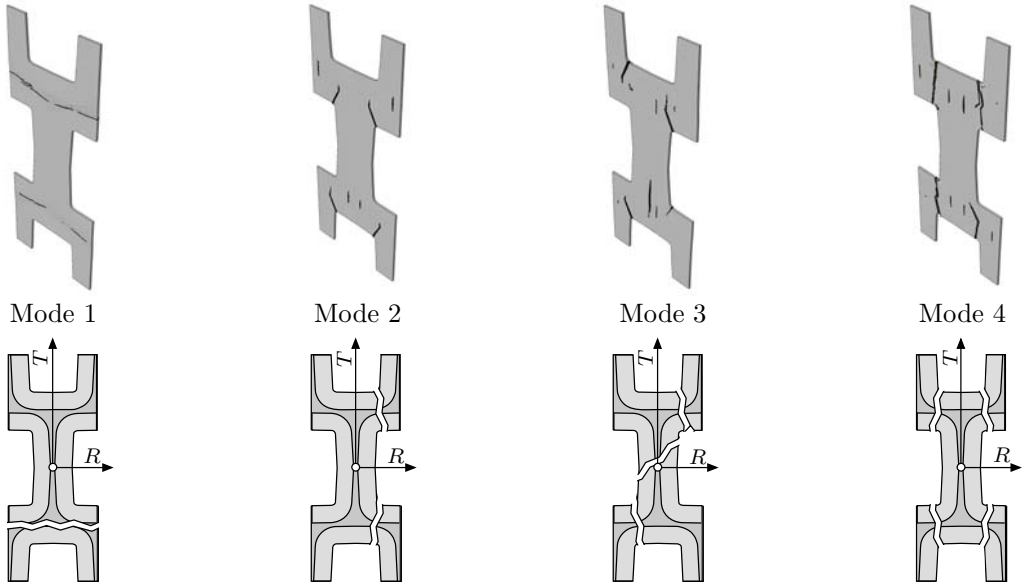

Figure 3.4: Distinction of four crack modes of a LW unit cell

By means of these timesteps it was possible to generate a complete failure criterion of the corresponding unit cell including the distinction of the four different crack modes.

On the basis of these figures, a specific cracking behavior and the corresponding cracking direction for the macroscopic area are assigned to each crack mode. Crack mode 1 occurs mainly at tension in T-direction, leading to a transection of the cell in R-direction. On the contrary, crack mode 2 occurs mainly at tension in R-direction, which ultimalely leads to a transection of the cell in T-direction. At crack mode 3, a transection of the cell at an angle between R- and T-direction occurs after simultaneous tension and shear loading in both directions. Crack mode 4 represents a special case, which occurs mainly at compressive load in T-direction leading to a transection of the cell walls and subsequently to a macroscopic direction of the crack in T-direction.

As mentioned before in Chapters 2.2.2 and 2.2.3, each material has its own failure criterion. If the value of one of these failure criteria reaches or exceeds 1, the elastic limit is reached and the crack initiation starts:

$$f(\boldsymbol{\sigma}) \leq 1 \tag{3.3}$$

Since two different failure criteria were used from the two modelled cell wall layers *ML* and *S2*, a simultaneous illustration of the failure index in both layers with the common available software tools was not possible. To overcome this deficiency and, thus, for an easier evaluation of the results, a new user subroutine to generate a user defined element output had to be defined (see Listing 3.1). With this *UVARM* the failure criterion is evaluated for each integration point of the two layers and can be illustrated now for the whole unit cell at once.

The images on the right in the Figures 3.5, 3.7, 3.9 and 3.11 show the wood cell in the cracked state, as well as the identifiable crack mode.

It is known that, on the basis of the macroscopic material model for wood, a radial load would first spread in the earlywood cell, which can be verified by the simulation results shown in Figure 3.5.

For the sake of clarity, out of the nine reaction forces (three forces at three master nodes) only the crucial ones in terms of their influence on the stress tensor were depicted (see Figures 3.6, 3.8, 3.10 and 3.12).

Listing 3.1: User value subroutine, uvarm.f

```
1         SUBROUTINE UVARM(UVAR,DIRECT,T,TIME,DTIME,CMNAME,ORNAME,
2         1 NUVARM,NOEL,NPT,LAYER,KSPT,KSTEP,KINC,NDI,NSHR,COORD,
3         2 JMAC,JMATYP,MATLAYO,LACCFLA)
4         INCLUDE 'ABA_PARAM.INC'
5 !
6 ! DEFINITIONS AND DIMENSIONS
7 !
8         real*8 UVAR,DIRECT,T,TIME,DTIME,COORD,ARRAY,S(6),PROPS(3)
              ,PROPS2(3),UVARtmp(3)
9         integer NUVARM,NOEL,NPT,LAYER,KSPT,KSTEP,KINC,NDI,NSHR,
              JARRAY,JRCD,JMAC,JMATYP,MATLAYO,LACCFLA
10        CHARACTER*80 CMNAME,ORNAME
11        CHARACTER*3 FLGRAY(15)
12        DIMENSION UVAR(NUVARM),DIRECT(3,3),T(3,3),TIME(2)
13        DIMENSION ARRAY(15),JARRAY(15),JMAC(*),JMATYP(*),COORD(*)
14 !
15 ! UVARM FOR ML LAYER
16 !
17        PROPS(1)=14.3
18        PROPS(2)=0
19        PROPS(3)=0
20 !
21        CALL GETVRM('S',ARRAY,JARRAY,FLGRAY,JRCD,JMAC,JMATYP,
              MATLAYO,LACCFLA)
22 !
23        S(1) = ARRAY(1)
24        S(2) = ARRAY(2)
25        S(3) = ARRAY(3)
26        S(4) = ARRAY(4)
27        S(5) = ARRAY(5)
28        S(6) = ARRAY(6)
29 !
30        IF (CMNAME .eq. 'ML') THEN
31          CALL SINV(S,SINV1,SINV2,3,3)
32          r=dsqrt((1d0/3d0)*((S(1)-S(2))**2+(S(2)-S(3))**2+(S(3)-
                S(1))**2+6*(S(4)**2+S(5)**2+S(6)**2)))
33          UVAR(1) = (r + PROPS(2)/(dsqrt(3d0))*SINV1)/(dsqrt(2d0)
                *PROPS(1))
34 !
35 ! UVARM FOR S2 LAYER
36 !
37        ELSE
```

```
38          PROPS2(1)= 175.
39              PROPS2(2)= 60.0
40              PROPS2(3)= 35.0
41  !
42              UVARtmp(1)=(S(3)/PROPS2(1))
43              UVARtmp(2)=(S(2)/PROPS2(2))
44              UVARtmp(3)=(S(4)/PROPS2(3))**2.0+(S(6)/PROPS2(3))**2.0
45  !
46              UVAR(1)=UVARtmp(1)
47              DO i = 2, 3
48                IF (UVAR(1).LT.UVARtmp(i)) THEN
49                  UVAR(1)=UVARtmp(i)
50                END IF
51              END DO
52            END IF
53  !
54            RETURN
55            END
```

The images on the left in Figures 3.5, 3.7, 3.9 and 3.11 show the specific unit cell for earlywood at the transition from linear elastic to plastic behavior. The color coding in the right images corresponds to the failure criterion of the respective material model.

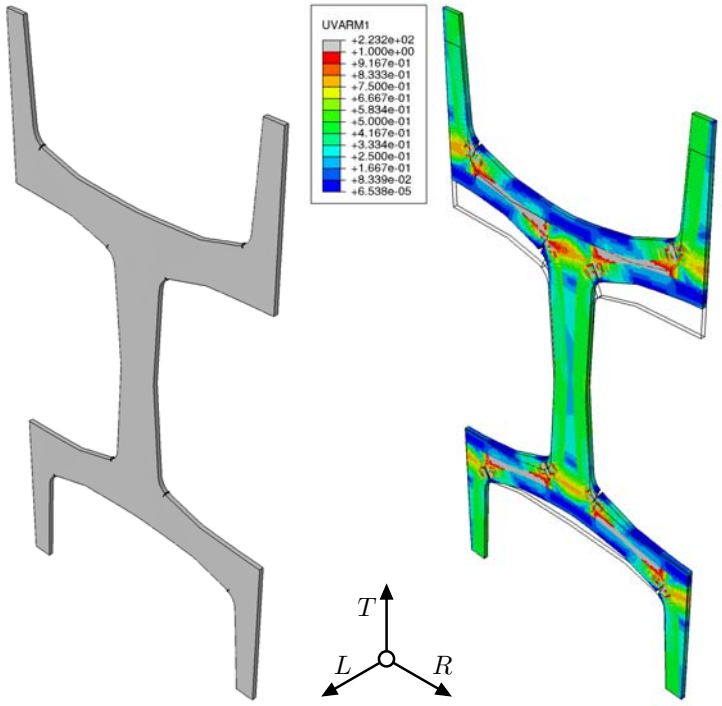

Figure 3.5: Initial cracks (on the left) and failure status at the last timestep (on the right) due to tensile loading in T-direction, resulting in crack mode 1

Figure 3.5 shows an earlywood cell with an applied load in T-direction only, ultimately leading to crack mode 1. The point of crack initiation is shown in the

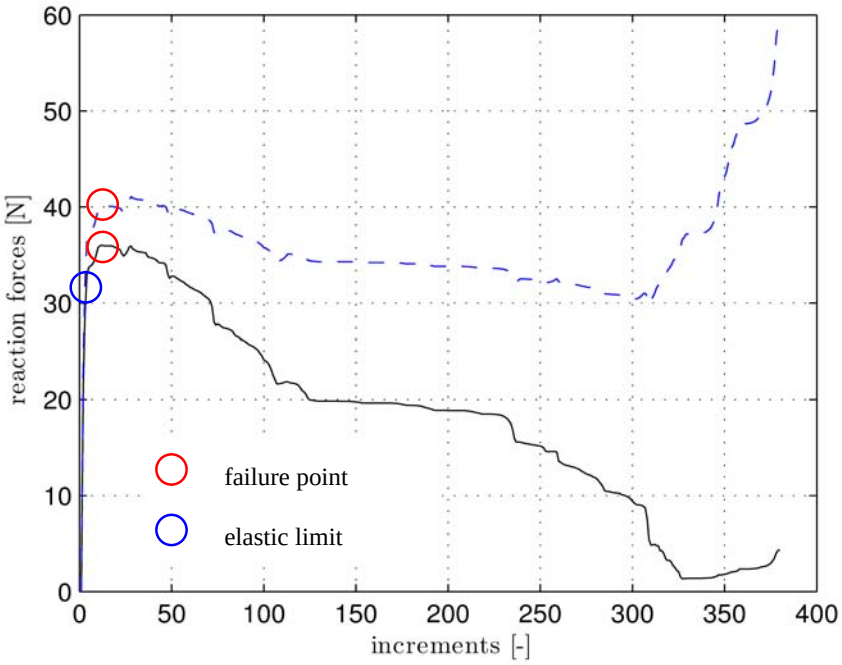

Figure 3.6: Reaction forces (RF_R^{SEB} blue and RF_T^{NWB} black line) of an earlywood cell with applied tensile loading in T-direction, representing crack mode 1.

image on the left and the most stressed areas after complete rupture are shown in the image on the right. This loadcase indicates that because of bending, the transition from the horizontal to the vertical part of the cell is the most stressed area and, therefore, the cracks have to occur there first. The moment of elastic limit and the point of failure is identified at the force-increment function, shown in Figure 3.6. The elastic limit is reached at the first point of transition of the force-increment function and the point of failure is located at the first increment where the force decreases.

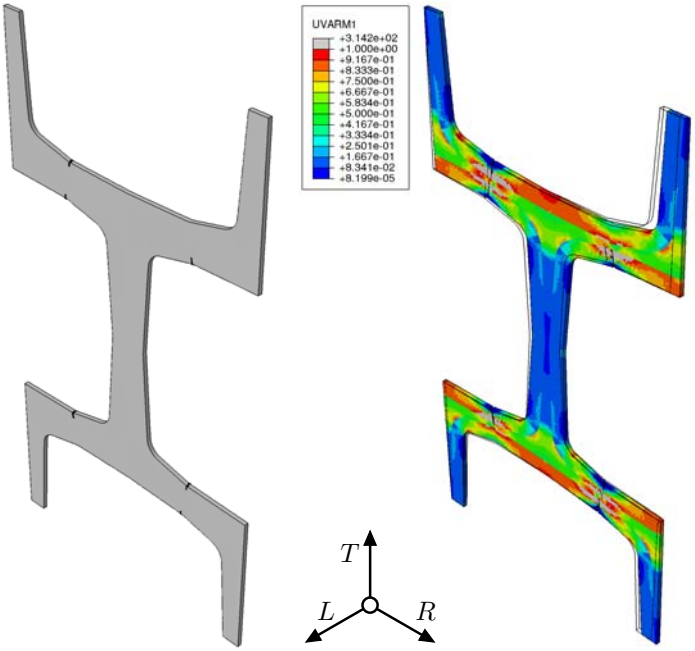

Figure 3.7: Initial cracks (on the left) and failure status at the last timestep (on the right) due to tensile loading in R-direction, resulting in crack mode 2

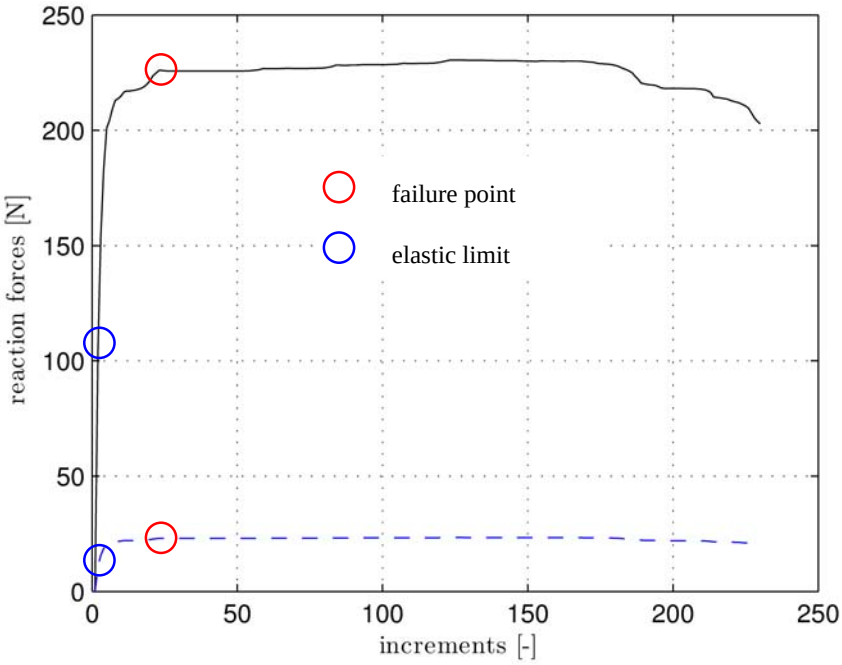

Figure 3.8: Reaction forces (RF_R^{SEB} blue and RF_T^{NWB} black line) of an earlywood cell with applied load, representing crack mode 2

Figure 3.7 shows an earlywood cell with an applied load in R-direction, ultimately leading to crack mode 2. The most stressed area of the cell occurs at its

thinnest position, where mainly stresses in normal direction to the cell wall appear. Figure 3.8 shows the corresponding force-increment function to the failure status in Figure 3.7 and the points of elastic limit and the point of failure.

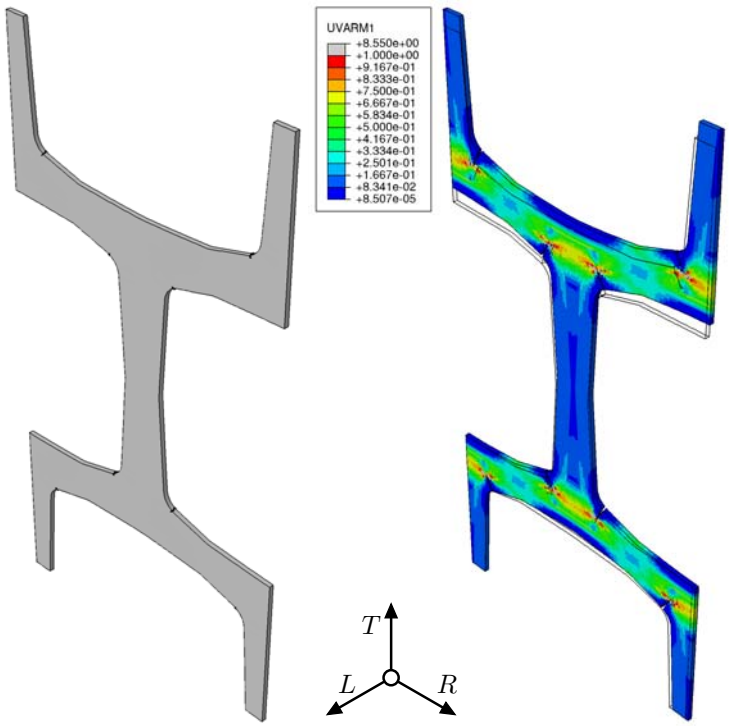

Figure 3.9: Initial cracks (on the left) and failure status at the last timestep (on the right) due to tensile loading in R and T-direction, resulting in crack mode 3

Figure 3.9 shows a cell with applied loads in R and T-direction leading to crack mode 3. The points of crack initiation are the same as shown in Figure 3.5 yet in case of the additional R-direction loading the rupture will end up in a mixed crack mode of mode 1 and mode 2, representing the so-called crack mode 3. The most stressed areas of the cell affect the middle lamella after the *S2* layer is severed. The force-increment function is shown in Figure 3.10 where the limits of elasticity and point of failure are read off.

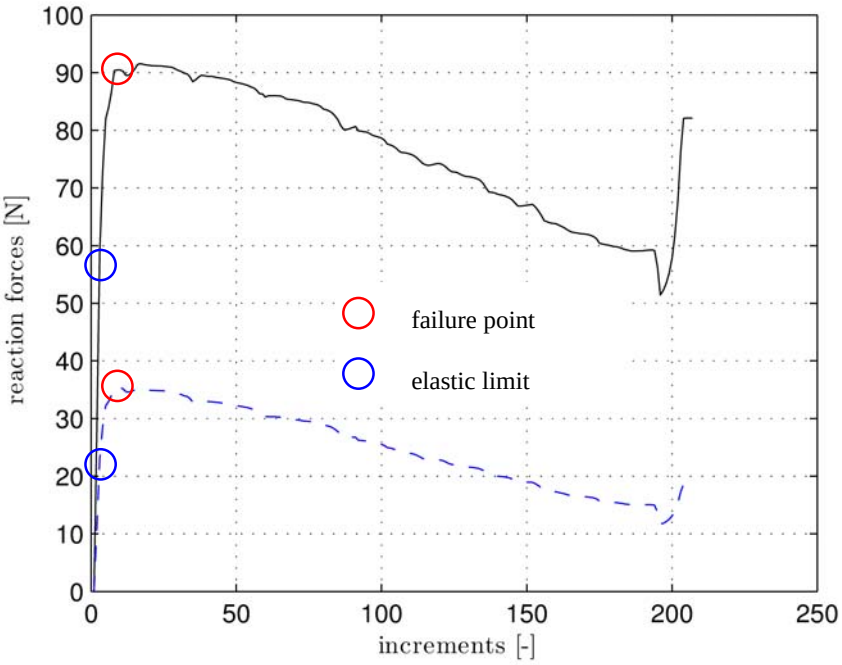

Figure 3.10: Reaction forces (RF_R^{SEB} blue and RF_T^{NWB} black line) of an earlywood cell with applied load, representing crack mode 3

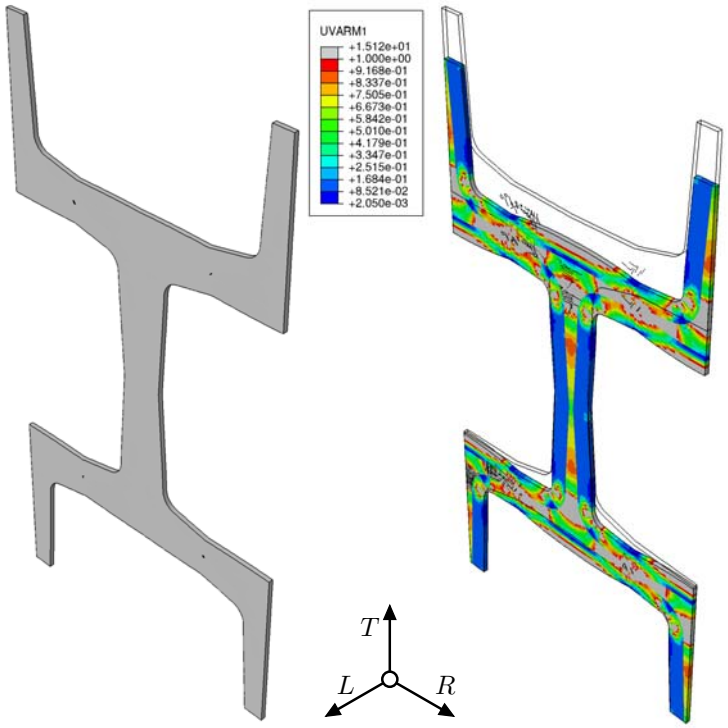

Figure 3.11: Initial cracks (on the left) and failure status at the last timestep (on the right) after a compressive load in T-direction, resulting in crack mode 4

To achieve crack mode 4 the earlywood cell has to be compressed in T-

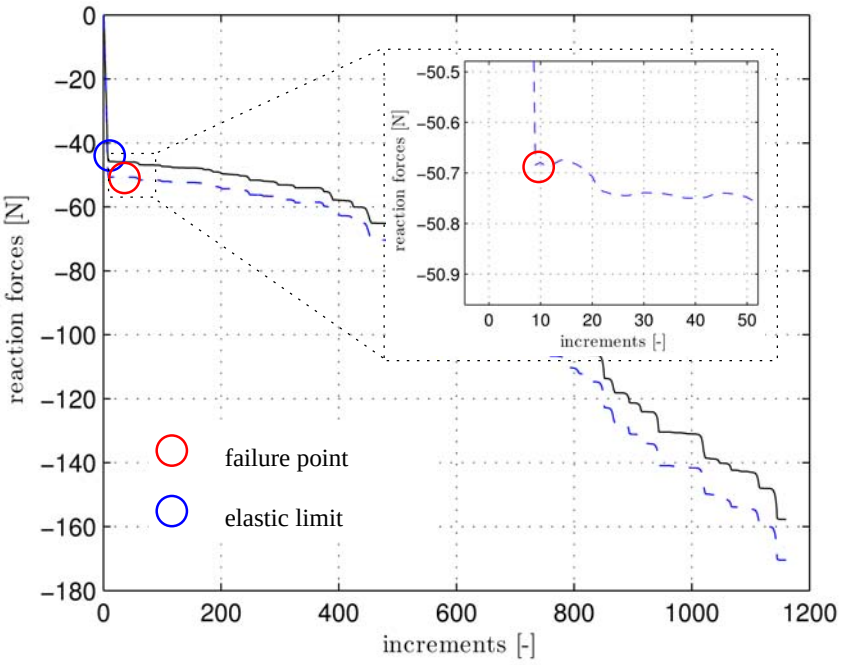

Figure 3.12: Reaction forces (RF_R^{SEB} blue and RF_T^{NWB} black line) of an earlywood cell with applied load, representing crack mode 4

direction. In that case the horizontal cell walls get severed by shear loads at their thinnest section. In contrast to the other crack modes, the crack initiation starts at the center of the *ML* instead of the *S2* layer surface (see Figure 3.11).

Using this force-increment function, shown in Figure 3.12, the elastic limit and likewise the point of failure could be detected.

In the same manner as the radially loaded earlywood cell, the latewood cell can be verified as well. In contrast to the earlywood cell, however, the cracks occur first in tangential direction through the middle lamella in the tangentially loaded latewood cell and spread to the adjacent cells. This can be observed based on the simulation shown in Figures 3.13, 3.15, 3.17 and 3.19.

In addition, based on the knowledge about the behavior of the macroscopic model, the initial crack direction can be controlled and, therefore, if radially loaded, results in crack mode 2. In contrast, regarding the tangentially loaded latewood cell, crack mode 1 occurs.

Figures 3.14, 3.16, 3.18 and 3.20 represent the force-increment functions in which the elastic region and the point of crack initiation were read off.

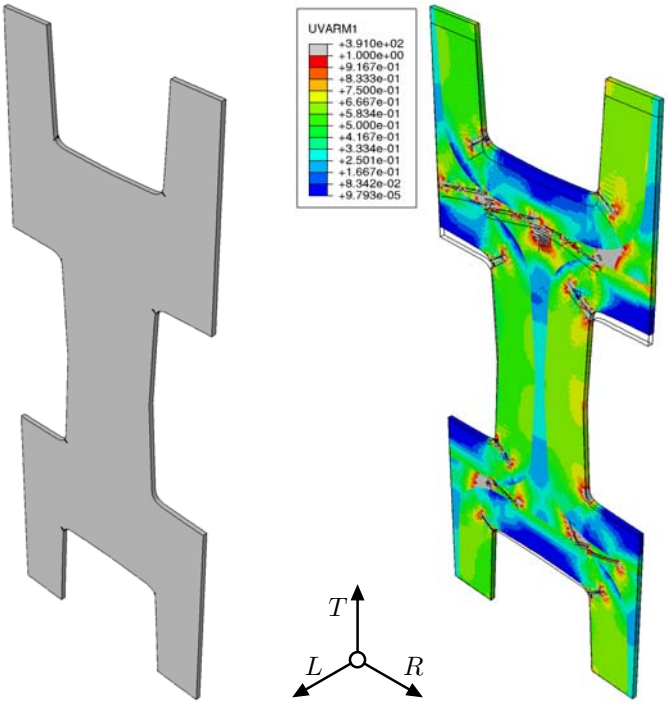

Figure 3.13: Initial cracks (on the left) and failure status at last timestep (on the right) due to tensile loading in T-direction resulting in crack mode 1

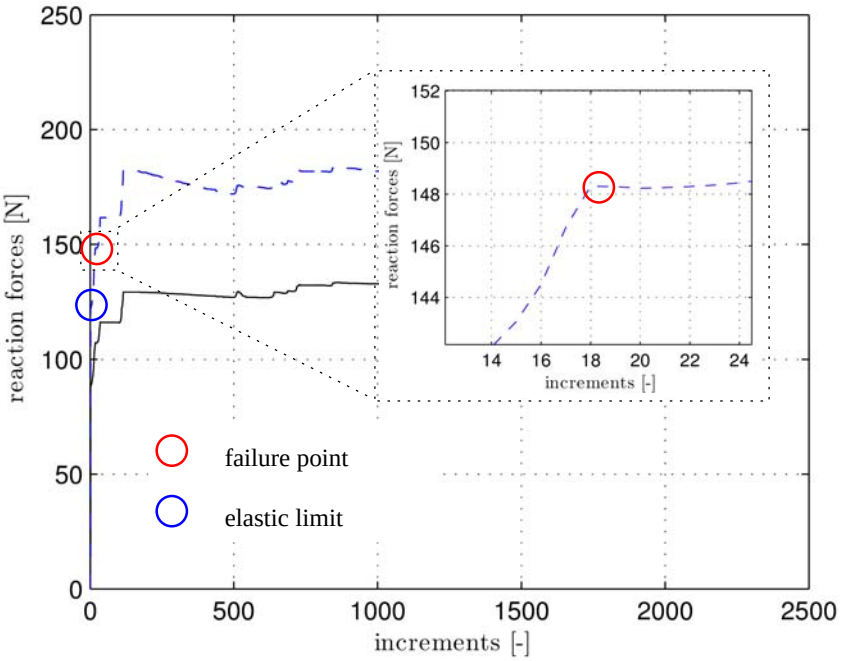

Figure 3.14: Reaction forces (RF_R^{SEB} blue and RF_T^{NWB} black line) of a latewood cell with applied load, representing crack mode 1

Crack mode 1, shown in Figure 3.13, occurs after an applied load only in

tangential direction. As mentioned before, this loadcase was used for verification of the material parameters, as from the macroscopic model it is known that a delamination of the cells has to be observed. The image on the left shows the points where the crack initiation starts, hence, it has to be pointed out that despite of the initiation on the *S2* layer's surface, after stress rearrangement the next cracks occur in the *ML* layer and after increasing loads it ultimately ruptures completely.

The force-increment function in Figure 3.14 shows the point of failure, and therefore it has to be pointed out that this point of failure is detected at the first decrease of the force-increment function. After this decrease it is still possible that the force raises again yet the initial point of failure remains at the first decrease of the force-increment function.

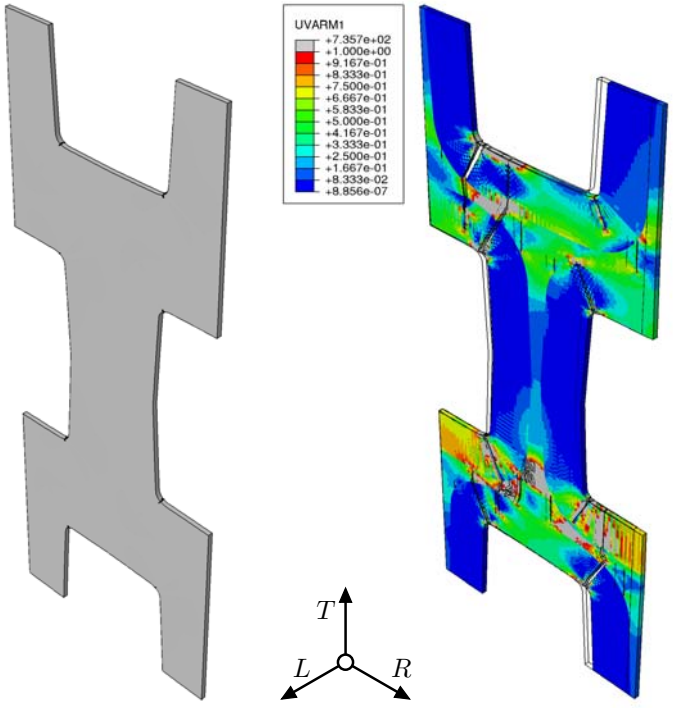

Figure 3.15: Initial cracks (on the left) and failure status at last timestep (on the right) due to tensile loading in R-direction resulting in crack mode 2

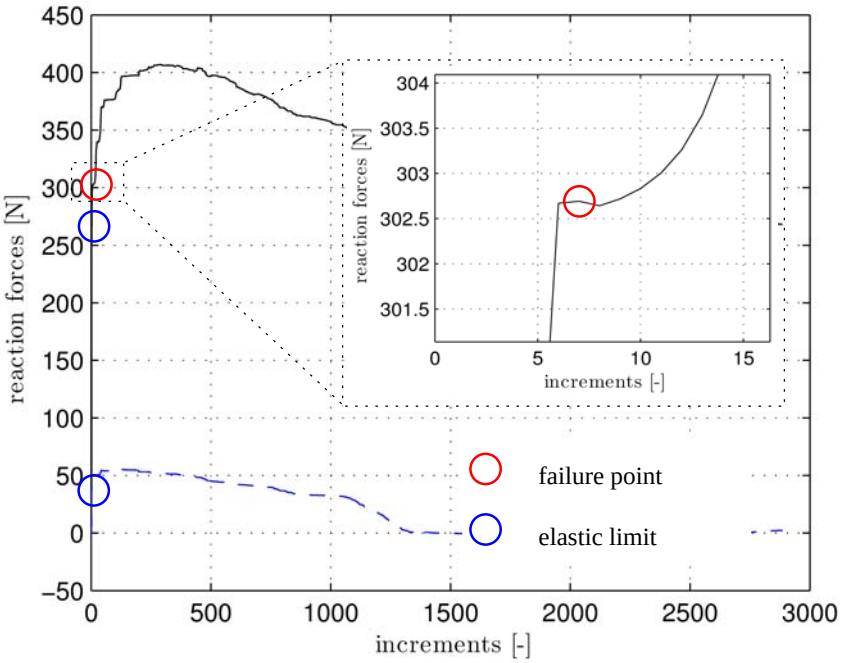

Figure 3.16: Reaction forces (RF_R^{SEB} blue and RF_T^{NWB} black line) of a latewood cell with applied load, representing crack mode 2

Figure 3.15 shows a latewood cell only radially loaded, ending up in crack mode 2. As depicted in the image on the left, the first cracks occur at the surface in the cell wall corner spreading through the whole cell wall until complete rupture. In Figure 3.16 the points of elastic limit and failure can be read off, especially in the enlargement it is identifiable that the first decrease of the force indicates the point of failure.

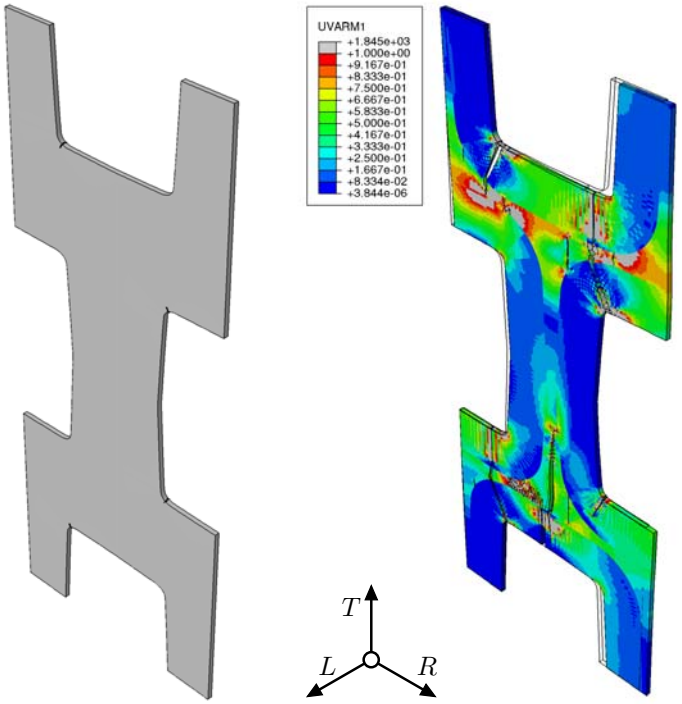

Figure 3.17: Initial cracks (on the left) and failure status at last timestep (on the right) due to shear loading in TL-plane resulting in crack mode 3

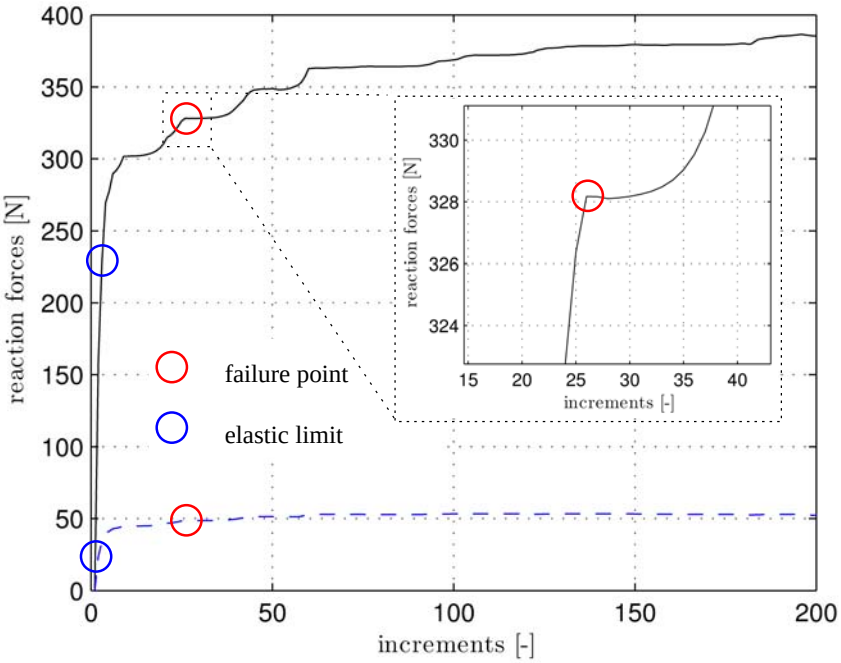

Figure 3.18: Reaction forces (RF_R^{SEB} blue and RF_T^{NWB} black line) of a latewood cell with applied load, representing crack mode 3

Crack mode 3 shown in Figure 3.17 could not be observed in the loadcase variations regarding RT-plane only. The additional simulation done with shear loads in the RL-plane led to the depicted crack mode. Applied with two different shear loads, the crack initiation starts in the middle lamella and finally the crack transects the cell completely. In Figure 3.18 elastic limit and failure are shown.

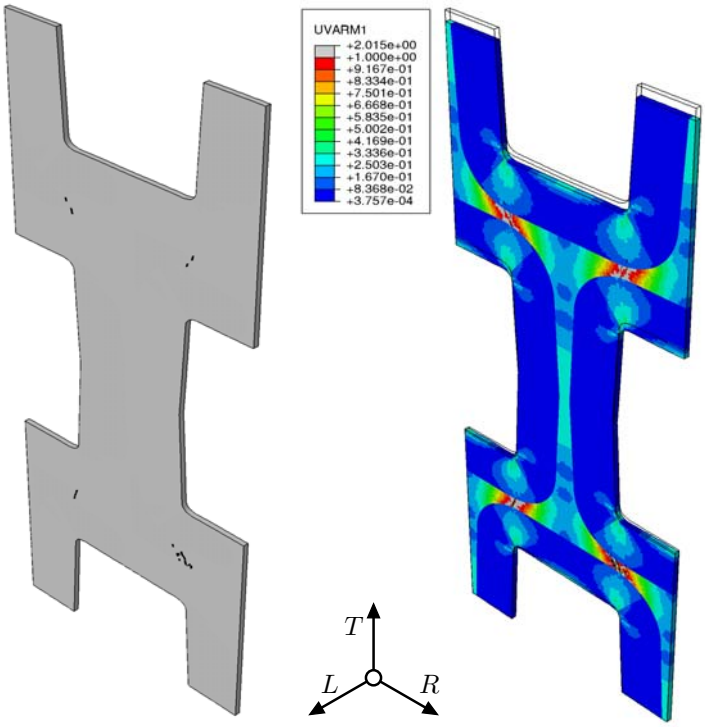

Figure 3.19: Initial cracks (on the left) and failure status at last timestep (on the right) due to compressive loading in T-direction resulting in crack mode 4

Crack mode 4 can only be observed with applied compressive loads in tangential direction, as shown in Figure 3.19. Depicted in the left image, the crack initiation starts in the middle lamella and spreads to the *S2* layer and finally through the whole cell wall in vertical direction.

Because of the different geometries of latewood and earlywood cells, the reaction forces of latewood cells reach much higher values.

An accurate verification of the hereby obtained limit stresses was not possible due to the lack of experimental data of the micromechanical model and could only be achieved by some interpretations of the macromechanical model.

Thus, the cracking behavior of a latewood cell in tangential direction was compared with the delamination of the cell walls at a limit stress of $\sigma_{TT} = 4.94 MPa$. This limit stress can be determined by tensile testing of a specimen in tangential direction [6].

Additionally, a comparison of the obtained stress tensors and as a result the stiffness and strength values for each cell type and the elastic stiffness and strength

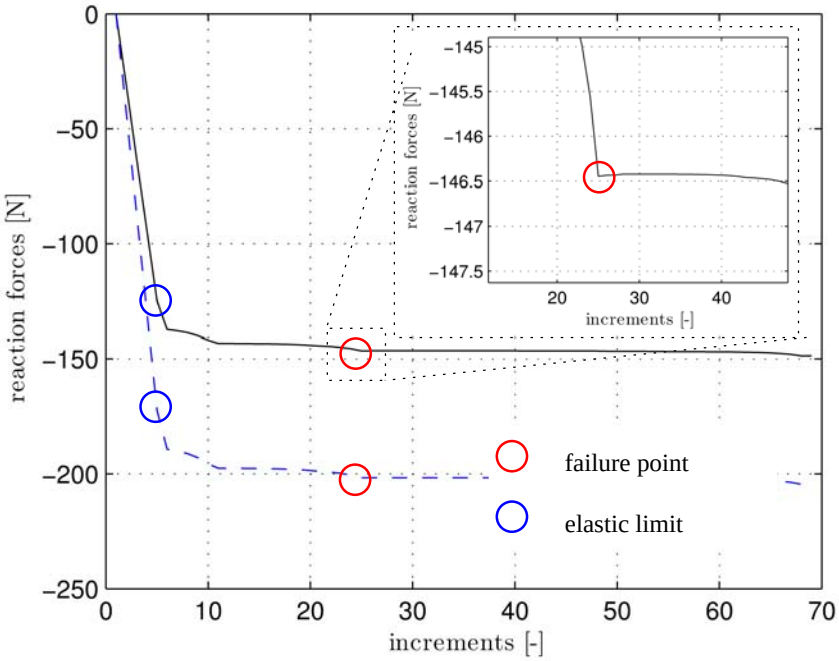

Figure 3.20: Reaction forces (RF_R^{SEB} blue and RF_T^{NWB} black line) of a latewood cell with applied load, representing crack mode 4

values of the macroscopic model is performed. Considering spruce with a density of $\rho = 400\ \frac{kg}{m^3}$, the areal amount of earlywood cells within an annual ring is about 80%. By means of this ratio the macroscopic elastic strength and stiffness of spruce could be determined. For an adequate verification of the macroscopic elastic limit values in R and T-direction, the two cells, their stresses and strains, respectively, had to be combined at the point of the elastic limit.

A load in R-direction leads to a serial response of the two cells, hence the macroscopic elastic limit is reached when the first elastic limit of either earlywood or latewood is reached. The elastic limit is reached in the earlywood cell first, with a strength value of:

$$f_{y,R}^{el} = \sigma_{RR}^{EW} = 5.56\text{MPa} \tag{3.4}$$

Because of a parallel behavior in T-direction, the macroscopic elastic strength has to be evaluated differently. This macroscopic strength value is obtained at the point with the lowest displacement of the elastic limit for either of both cell types. By means of this displacement the stress value of the two cells can be calculated. Since spruce with an areal ratio of 80%/20% was used, this factor had to be applied at the stress values, resulting in:

$$f_{y,T}^{el} = 0.2\sigma_{TT}^{EW} + 0.8\sigma_{TT}^{LW} = 2.53\text{MPa} \tag{3.5}$$

with the stress values:

$$\sigma_{TT}^{EW} = 0.82\text{MPa} \quad \text{and} \quad \sigma_{TT}^{LW} = 9.39\text{MPa} \tag{3.6}$$

The lower value of the two strength values obtained above, can be explained by the geometry of both cells. Assuming that cracks will first occur in cells with the weakest cell shape, those cells were used as the basis for this evaluation. Therefore, it is obvious that the macroscopic limit has to be lower than measured limits observed experimentally.

Not only strength values for a macroscopic model could be obtained, but also the moduli of elasticity for R, T and L-direction were evaluated.

First the stiffness matrix of each cell had to be determined for a definition of the macroscopic modulus of elasticity depending on the direction (E_R, E_T and E_L). Therefore six different loadcases for each cell were used, whereby all components of the stiffness tensor could be identified (see Equation (2.1) and (2.2) introduced in Chapter 2.2.1 as an example).

$$\mathbb{C} = \mathbb{D}^{-1}. \tag{3.7}$$

Using equation (3.7) all components of the compliance matrix were defined and finally the moduli of elasticity split by direction and cell type were obtained (3.8) and (3.9).

$$E_R^{EW} = 363.4\text{MPa}, \quad E_T^{EW} = 192.4\text{MPa}, \quad E_L^{EW} = 3969.3\text{MPa} \tag{3.8}$$

$$E_R^{LW} = 665.8\text{MPa}, \quad E_T^{LW} = 871.8\text{MPa}, \quad E_L^{LW} = 9259.3\text{MPa} \tag{3.9}$$

For the global moduli of elasticity, earlywood and latewood values had to be combined. This kind of combination depends on the direction, which finally leads to the macroscopic moduli of elasticity listed below (3.10).

$$E_R^{macro} = 570.8\text{MPa}, \quad E_T^{macro} = 328.3\text{MPa}, \quad E_L^{macro} = 5026.5\text{MPa} \tag{3.10}$$

For a comparison, the moduli of elasticity obtained by the micromechanic model of Hofstetter et al. [9] can be used:

$$E_R^{MMM} = 550.93\text{MPa}, \quad E_T^{MMM} = 365.78\text{MPa}, \quad E_L^{MMM} = 12203\text{MPa} \tag{3.11}$$

It can be seen that the values obtained from this unit cell approach possess a lower value than those achieved by Hofstetter et al. This can be explained by the use of the weakest unit cell shape in this approach, especially for T and L-direction. The higher value for the modulus of elasticity in R-direction might be explained by the bigger length l_R^{LW} compared to the one used in the micromechanical model by Hofstetter et al.

Based on the four different crack modes shown in Figures 3.3 and 3.4, the aggregated stress tensors for earlywood and latewood were mapped and divided into respective stress planes. For each individually computed model a decisive crack

mode was assigned. The failure functions shown in Figure 3.21 and Figure 3.22 can be compared with a Tsai-Wu failure criterion. As this comparison of the Tsai-Wu failure criterion with all summarized failure modes of the earlywood and latewood cells follow at the end of this section, only the failure modes in σ_{RR}-σ_{TT} and σ_{RR}-τ_{RT} planes are depicted below.

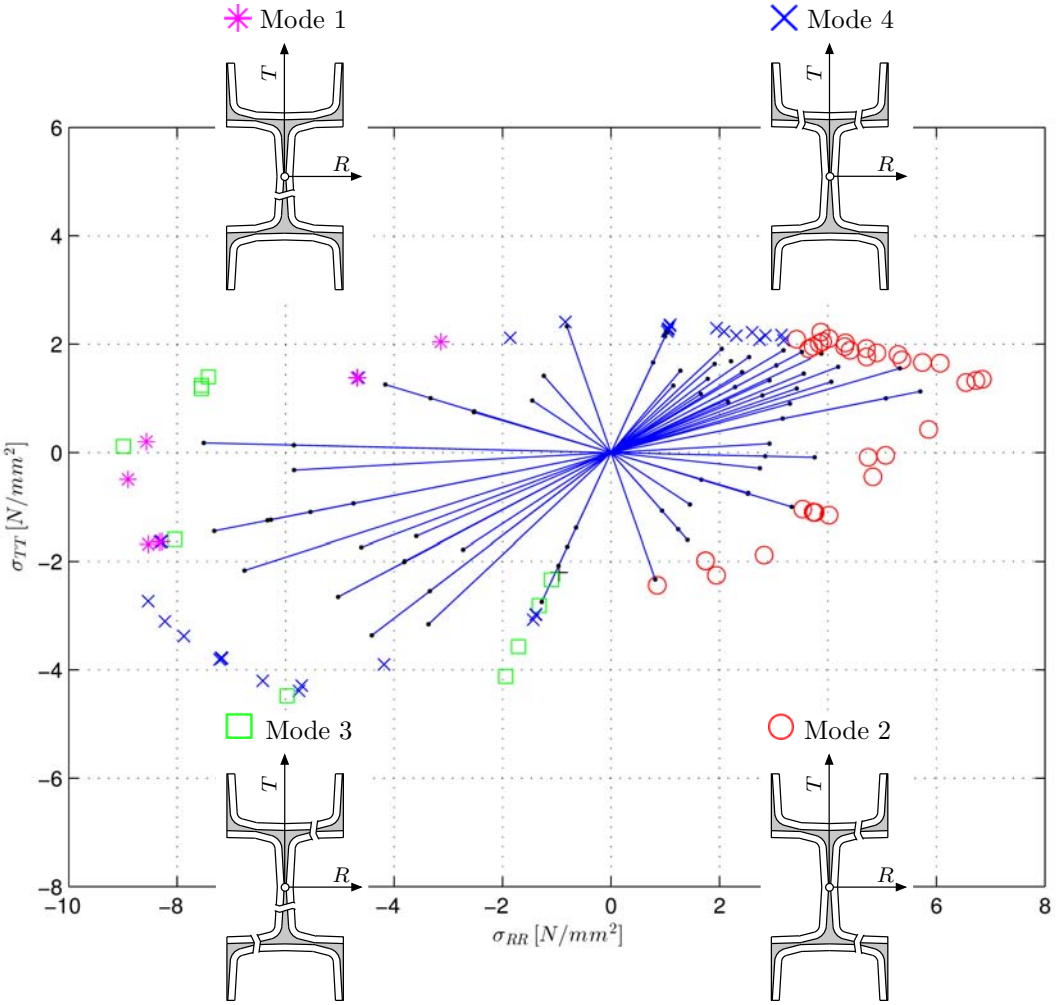

Figure 3.21: Failure modes of an earlywood cell

Figure 3.21 shows a summary of all loadcases applied for the earlywood cell. The point from elasticity to plasticity is pictured with a black dot and a blue solid line. Four different markers were used to indicate the point of complete rupture and to differ the four crack modes. Additionally, it can be observed that crack mode 2 only occurs if load is applied mainly radially. This is the only crack mode which can be differentiated completely by means of the applied load. The three remaining crack modes can't be detected completely by means of the applied loads, but a plain trend is shown, e.g. compression in radial and tangential direction will mainly lead to crack mode 3, yet if the tangential compression increases, a transition to crack mode 4 is identifiable. In a similar

manner, a change between crack modes 1, 2 and 3 can be observed, especially, when compression loads in T-direction are applied. For loadcases with tangential tension only crack mode 4 is detectable.

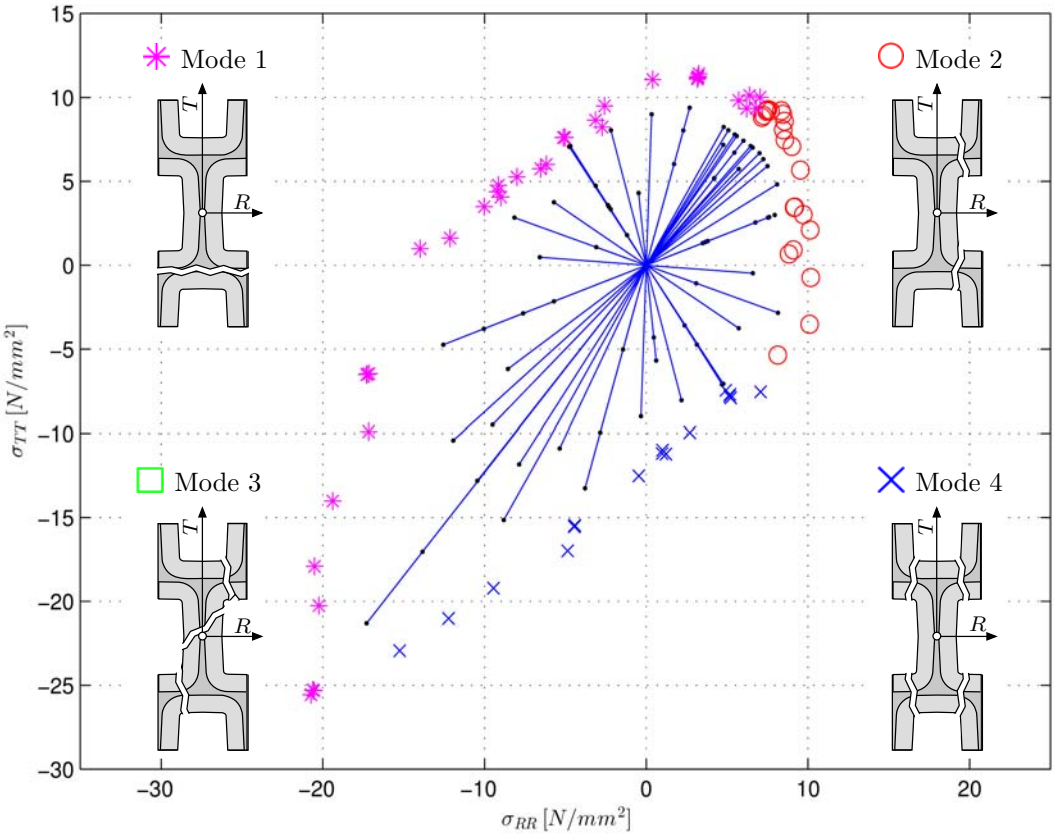

Figure 3.22: Failure modes of a latewood cell

Figure 3.22 shows a summary of all loadcases applied for the latewood cell. The point of transition from elasticity to non-linearity is pictured with a black dot and a blue solid line. An interesting point in the figure is that crack mode 3 did not occur for loadcases regarding RT-plane only. A clear distinction between crack modes and applied loads is identifiable. In that case crack mode 2 only occurs in loadcases with applied tension in radial direction or in combination with tangential tension. Crack mode 4 mainly belongs to an applied compression load in T-direction and crack mode 1 belongs to applied tension loads in T-direction. A transition from crack mode 4 to crack mode 1 is apparent at the point of maximum pressure in both directions.

In Figures 3.21 and 3.22 the different shape in comparison to the Tsai-Wu failure criteria is shown and therefore the main reasons can be explained as followed. The crack behavior of the earlywood cell does not change abruptly, since the thin cell walls can not head to rapid change of the crack directions and subsequently evoke peaks in the failure surface. Furthermore, these differences such as the sharp transition at the compression-compression sector can be observed in Figure 3.22. This peak occurs due to the transition between crack mode 1 to

crack mode 4 or reversely. The transition from crack mode 2 to crack mode 4 does not evoke such a peak, which can be explained by a similar crack manner. One of the interesting parts of this unit cell approach is the different rotation of the failure surface for the two cell types. In case of the thicker cell walls the latewood cell is able to absorb higher values of pressure than the earlywood cell.

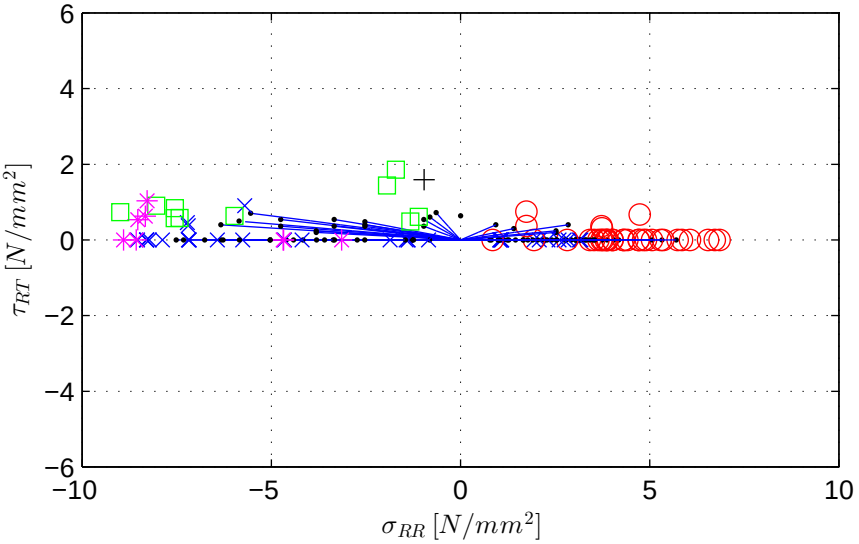

Figure 3.23: Stress and shear components of an earlywood cell

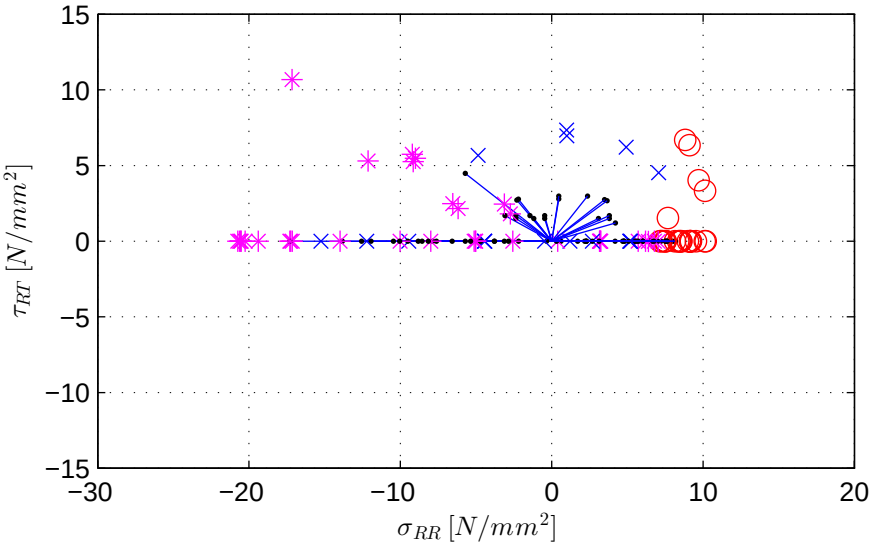

Figure 3.24: Stress and shear components of a latewood cell

Figures 3.23 and 3.24 show the σ_{RR}-τ_{RT} stress plane as a result of the applied loads in RT-plane. To receive all remaining shear components of the stress tensor $\boldsymbol{\sigma}$, loads in TL and LR-plane are necessary. The identification of the models with their respective crack modes indicates the significance of the special crack pattern

regarding its corresponding stress state. Analogously, the analysis for the load combination of the latewood and its crack patterns was undertaken.

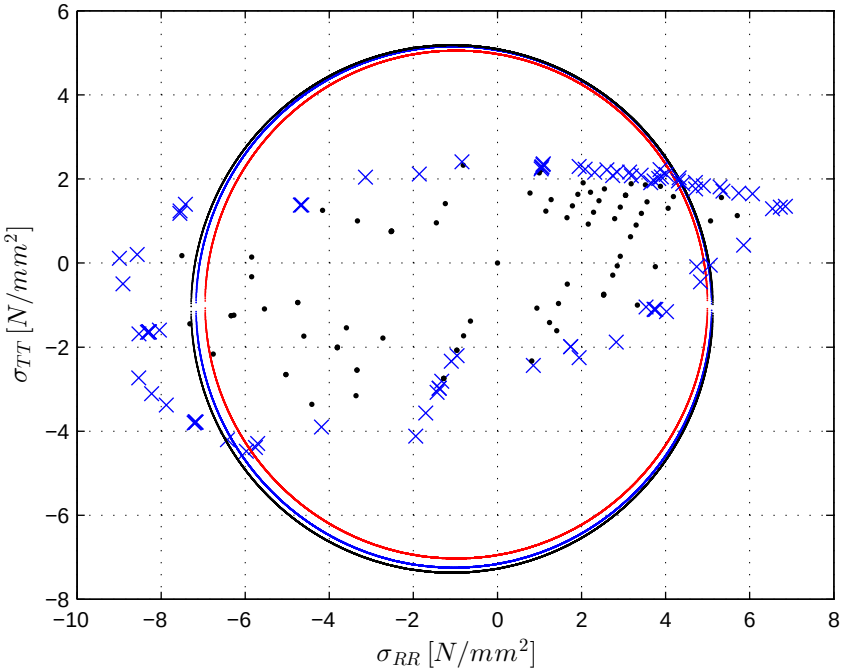

Figure 3.25: Comparison of numerical results for EW to the TSAI-WU criterion for clear wood (spruce) in RT-plane; $\sigma_{LL,min} = -6.86$ (red), $\sigma_{LL,0} = 0$ (blue), $\sigma_{LL,max} = 5.05$ (black) and $\sigma_{RT} = \sigma_{TL} = \sigma_{LR} = 0$ (all) [MPa]

Figures 3.25, 3.26 and 3.27 show the TSAI-WU failure criterion for spruce pictured in three different stress planes, showing three different cuts of the TSAI-WU ellipsoid for a constant third stress component, e.g. σ_{LL} as third stress component for the σ_{RR}-σ_{TT} stress plot. Since a TSAI-WU failure criterion represents a failure surface in shape of an ellipsoid, one single criterion is not able to fit all the points of failure received from the FEM simulation of the two used unit cells. Hence, a more or less wide deviation has to be accepted. For a better representation of the unit cells' behavior, at least three different TSAI-WU failure criteria have to be formulated for each cell.

In case of an accumulation of different loadcases regarding RT-plane only, all points of failure lie in a plane in the σ_{RR}-σ_{TT}-σ_{LL} stress space. In order to depict a three dimensional figure of failure points, additional loadcases including loads in L-direction must be examined.

Figure 3.25 shows the points of failure compared to the TSAI-WU failure criterion for spruce, whereby the red depiction shows a cross section of this criterion at a constant stress state $\sigma_{LL} = -6.86$MPa and the black depiction shows a cross section at $\sigma_{LL} = 5.05$MPa. The two mentioned stress values correspond to the minimum and maximum value of the failure points.

In the same manner the Figures 3.26 and 3.27 depict the cross section of the TSAI-WU failure criterion.

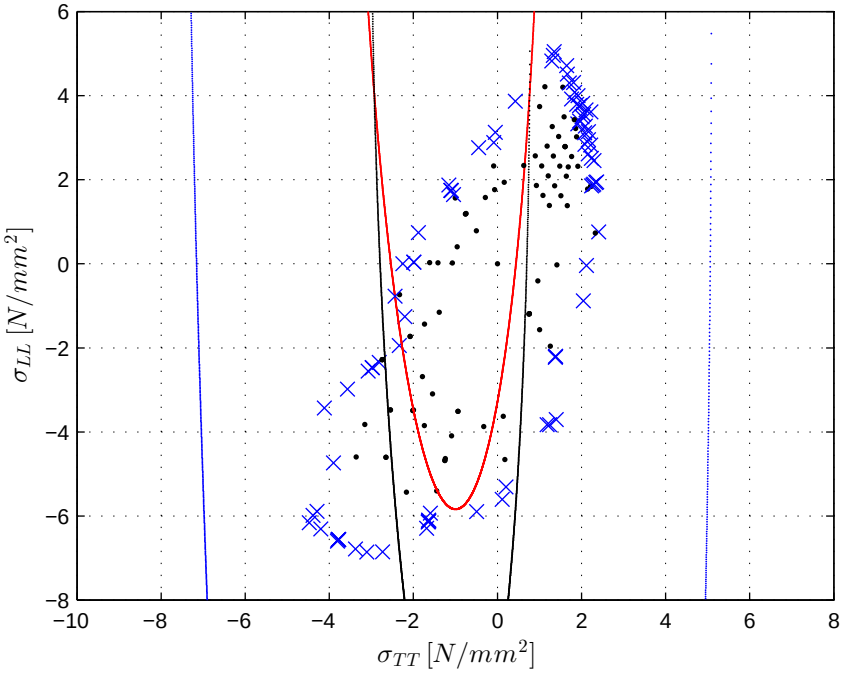

Figure 3.26: Comparison of numerical results for EW to the TSAI-WU criterion for clear wood (spruce) in TL-plane; $\sigma_{RR,min} = -7.0$ (red), $\sigma_{RR,0} = 0$ (blue), $\sigma_{RR,max} = 5.0$ (black) and $\sigma_{RT} = \sigma_{TL} = \sigma_{LR} = 0$ (all) [MPa]

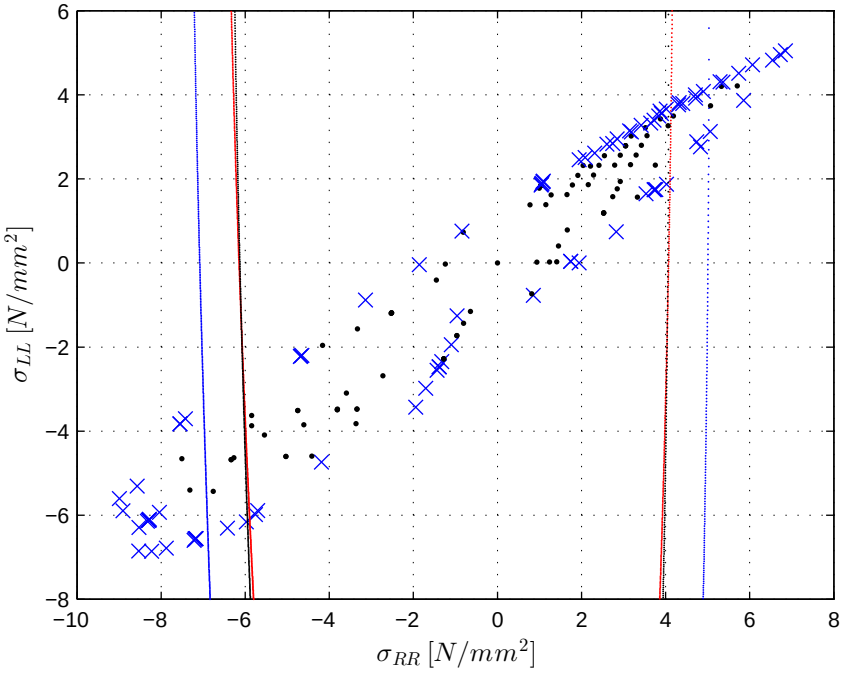

Figure 3.27: Comparison of numerical results for EW to the TSAI-WU criterion for clear wood (spruce) in LR-plane; $\sigma_{TT,min} = -4.48$ (red), $\sigma_{TT,0} = 0$ (blue), $\sigma_{TT,max} = 2.41$ (black) and $\sigma_{RT} = \sigma_{TL} = \sigma_{LR} = 0$ (all) [MPa]

It is clearly identifiable that the depiction of the TSAI-WU failure criterion can not display the accumulation of all failure points accurately, which can be explained by comparing the macroscopic model with the failure criterion of an earlywood cell. Yet it must be noted that the range of the macroscopic model is located in the same range.

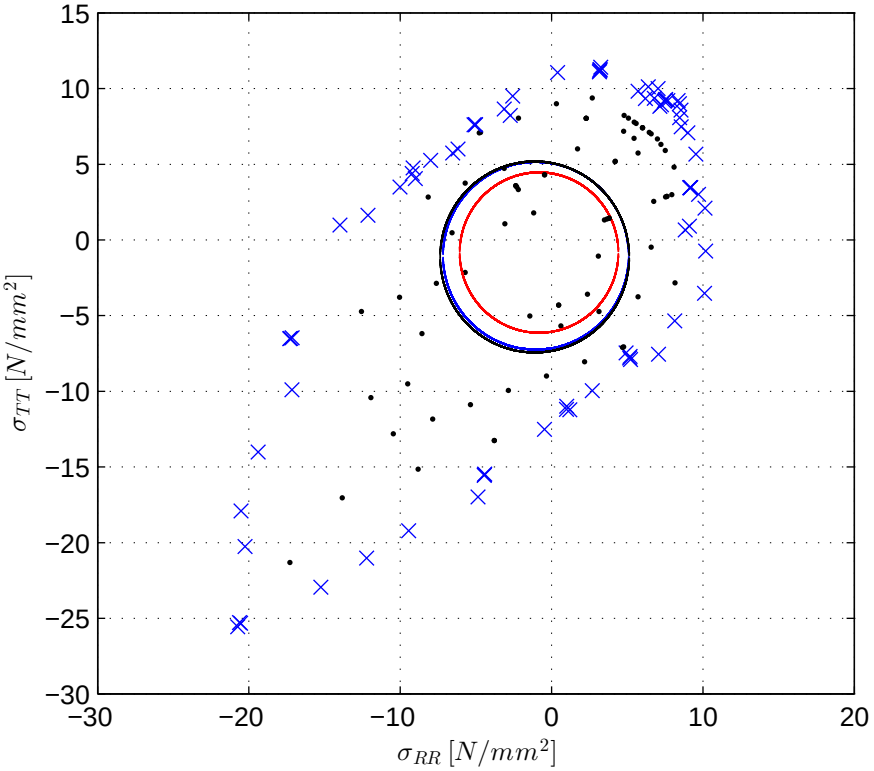

Figure 3.28: Comparison of numerical results for LW to the TSAI-WU criterion for clear wood (spruce) in RT-plane; $\sigma_{LL,min} = -24.32$ (red), $\sigma_{LL,0} = 0$ (blue), $\sigma_{LL,max} = 9.22$ (black) and $\sigma_{RT} = \sigma_{TL} = \sigma_{LR} = 0$ (all) [MPa]

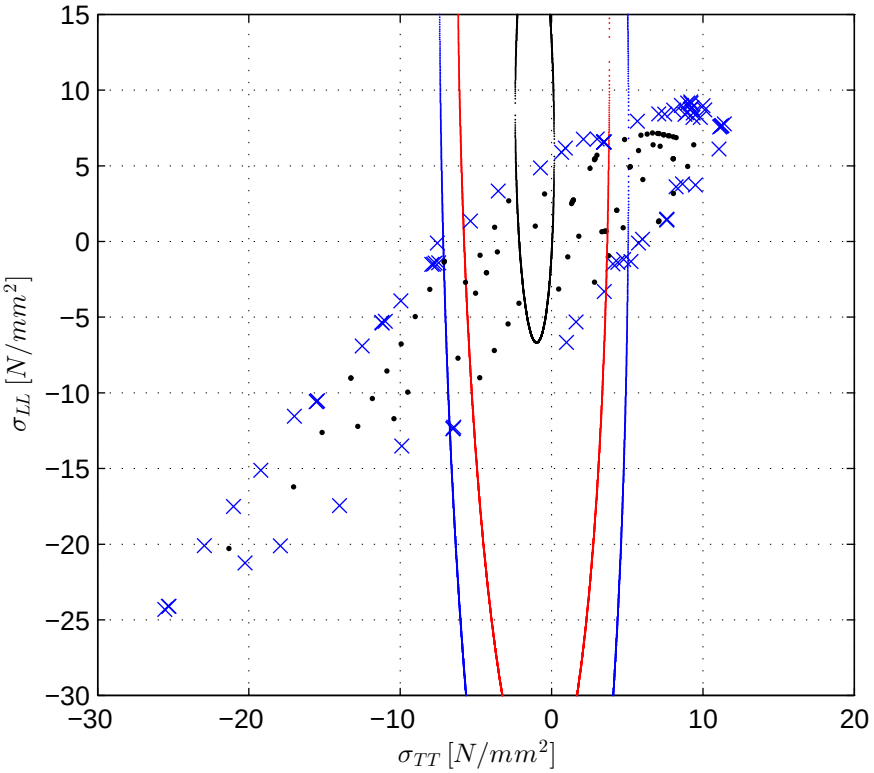

Figure 3.29: Comparison of numerical results for LW to the TSAI-WU criterion for clear wood (spruce) in *TL*-plane; $\sigma_{RR,min} = -5.0$ (red), $\sigma_{RR,0} = 0$ (blue), $\sigma_{RR,max} = 5.0$ (black) and $\sigma_{RT} = \sigma_{TL} = \sigma_{LR} = 0$ (all) [MPa]

Figures 3.28, 3.29 and 3.30 show the TSAI-WU failure criterion for latewood, pictured in three different stress planes, showing three different cuts of the TSAI-WU ellipsoid of the corresponding third stress component.

As the comparsion of the TSAI-WU failure criterion done with the crackmodes of earlywood pictured all points of failure in a plane in the stress space, the same is identifiable for all points of failure of latewood.

Table 3.1: Overview of TSAI-WU tensor components

	a_{RR}	a_{TT}	a_{LL}	b_{RRRR}	b_{TTTT}	b_{LLLL}
Spruce	0.0585	0.0578	-0.00527	0.0282	0.0276	0.00023
	b_{RRTT}	b_{TTLL}	b_{LLRR}	b_{RTRT}	b_{TLTL}	b_{LRLR}
Spruce	0.0	0.00024	0.00024	0.0254	0.00295	0.00295

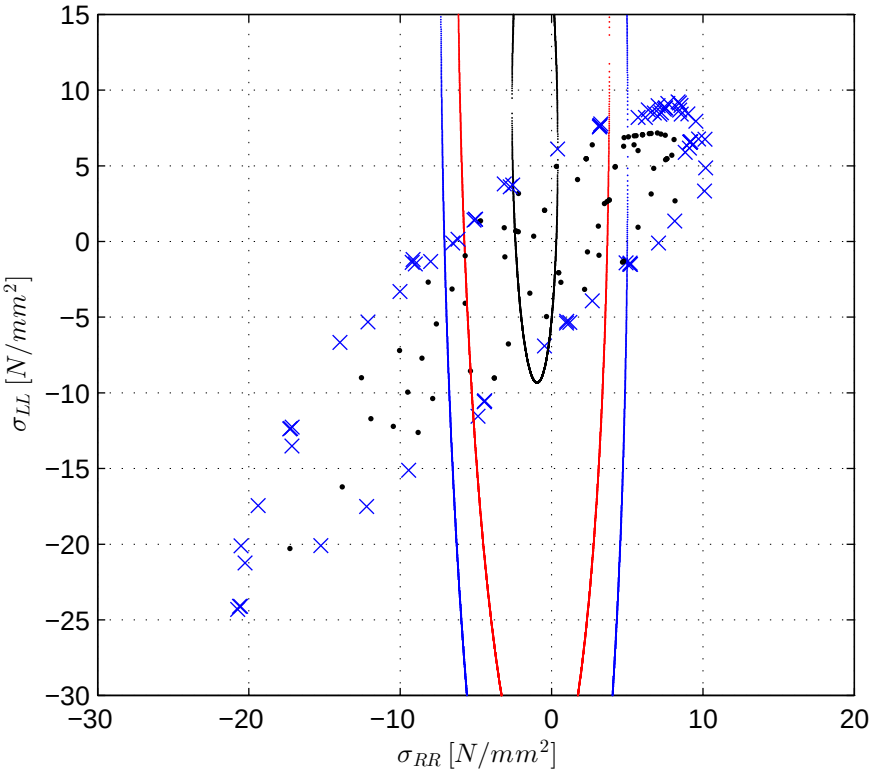

Figure 3.30: TComparison of numerical results for LW to the Tsai-Wu criterion for clear wood (spruce) in LT-plane; $\sigma_{TT,min} = -5.0$ (red), $\sigma_{TT,0} = 0$ (blue), $\sigma_{TT,max} = 5.0$ (black) and $\sigma_{RT} = \sigma_{TL} = \sigma_{LR} = 0$ (all) [MPa]

3.3 Summary and Conclusion

Within this thesis, cracking of clear wood is investigated at the cell level. For this purpose, a unit cell for early- and latewood was defined and a Python script was coded to allow for an automatic generation of cell geometries. In a further step, periodic boundary conditions were applied to these unit cells and by using the commercial Finite Element code *Abaqus* ™, numerical simulations for different load combinations were performed. Cracking of the considered two cell wall layers was modelled by an extended Finite Element approach.

Based on the obtained results the following conclusions can be drawn:

- With the implementation of a crack initiation and crack direction criterion as user subroutine in *Abaqus* ™, the transversal isotropic nature of the S2 layer could be taken into account and cracking of this layer could be considered appropriately.
- With this approach it was possible to reproduce/identify basic crack modes for both early- and latewood cell types individually, which can be found in literature.

- By applying different load combinations on the unit cells, failure surfaces could be identified and it was possible to assign the obtained crack modes to stress regions on them.
- A comparison of the obtained failure surfaces with the well-known failure criterion according to TSAI-WU, which is often used to describe plastic onset of clear wood, has shown the limitations of an analytical single-surface plasticity criterion.

In summary, it can be stated that the proposed numerical approach has great potential to contribute to a better understanding of crack processes in clear wood. The automatic generation of the cell geometry and the periodic boundary conditions allows for an easy adoption of the cell type, and thus, the investigation of different clear wood densities, species, et cetera.

Future investigations will focus on the reproduction of the obtained failure surfaces with TSAI-WU failure criteria. This information will then be transferred to the next higher scale, at which early- and latewood layers are considered as homogeneous materials. Finally, an effective failure criterion, including crack directions, at the clear wood scale should be obtained, allowing for an appropriate consideration of cracking mechanisms within timber boards and wood-based products.

Bibliography

[1] Abaqus Manual. *Dassault Systemes, Abaqus User's Manual (Version 6.12)*, 2012.

[2] T. K. Bader and K. Hofstetter. Micromechanical model for effect of thermal degradation of wood and macroscopic mechanical properties. *Technical Report, Task 1.3 in WoodWisdom-Net FireInTimber*, 2009.

[3] T. K. Bader, K. Hofstetter, C. Hellmich, and J. Eberhardsteiner. The poroelastic role of water in cell walls of the hierarchical composite "softwood". *Acta Mechanica*, 217(1-2):75–100, 2011.

[4] G. Calanotti, P. P. Camanho, and A. T. Marques. Three-dimensional failure criteria for fiber-reinforced laminates. *Composite Structures*, 95:63–79, 2013.

[5] Q. Deng, S. Li, and Y. Chen. Mechanical properties and failure mechanism of wood cell wall layers. *Computational Material Science*, 62:221–226, 2012.

[6] J. Eberhardsteiner. *Mechanisches Verhalten von Fichtenholz*. Springer WienNewYork, 2002.

[7] M. Fleischmann. *Numerische Berechnung von Holzkonstruktionen unter Verwendung eines realitätsnahen orthotropen elasto-plastischen Werktstoffmodells*. PhD thesis, Technische Universität Wien, 2005.

[8] S. Gloimüller. *Multiscale modeling and experimental investigation of the hygroexpansion behavior of softwood*. PhD thesis, Technische Universität Wien, 2012.

[9] K. Hofstetter, C. Hellmich, and J. Eberhardsteiner. Development and experimental validation of a continuum micromechanics model for the elasticity of wood. *European Journal of Mechanics - A/Solids*, 24:1030–1053, 2005.

[10] K. Hofstetter, C. Hellmich, and J. Eberhardsteiner. Micromechanical modeling of solid-type and plate-type deformation patterns within softwood materials. a review and an improvement approach. *Holzforschung*, 61:343–351, 2006.

[11] R. Keylworth. Die anisotrope Elastizität des Holzes und der Lagenhölzer. *VDI Forschungsheft*, 430, 1951. In German.

[12] F. Kollmann. *Technologie des Holzes und der Holzwerkstoffe*, volume 1. Verlag Springer, Berlin, Heidelberg, New York, 2nd edition, 1951. In German.

[13] H. Kühne. Über den Einfluss von Wassergehalt, Raumgewicht, Faserstellung und Jahrringstellung auf die Festigkeit und Verformbarkeit schweizerischen Fichten-, Tannen-, Lärchen-, Rotbuchen- und Eichenholzes. *EMPA-Bericht*, 183, 1955. In German.

[14] M. Lukacevic and Füssl. Numerical simulation tool for wooden boards with a physically based approach to identify structuraal failure. *European Journal of Wood and Wood Products*, to be published, 2013.

[15] H. Mang and G. Hofstetter. *Festigkeitslehre*. Springer WienNewYork, 2004.

[16] Matlab Documentation. *MathWorks, Matlab Documentation (Version R2013a)*, 2013.

[17] L. Mishnaevsky Jr. and H. Qing. Micromechanical modelling of mechanical behaviour and strength of wood: State-of-the-art review. *Computational Material Science*, 44:363–370, 2008.

[18] D. H. Pahr and P. K. Zysset. Influence of boundary conditions on computed apparent elastic properties of cancellous bone. *Biomech Model Mechanobiol*, 7:463–476, 2008.

[19] A. Puck. *Festigkeitsanalyse von Faser-Matrix-Laminaten*. Hanser, 1996. In German.

[20] A. Puck and H. Schürmann. Failure analysis of FRP laminates by means of physically based phenomenological models. *Composite Science and Technology*, 58:1045–1067, 1998.

[21] A. Puck and H. Schürmann. Failure analysis of FRP laminates by means of physically based phenomenological models. *Composite Science and Technology*, 58:1045–1067, 1998.

[22] S. Tsai and E. Wu. A general theory of strenght for anisotropic materials. *Journal of Composite Materials*, 5(1):58–80, 1971.

[23] F. K. Wittel, G. Dill-Langer, and B-H. Kröplin. Modeling of damage evolution in soft-wood perpendicular to grain by means of a discrete element approach. *Computational Material Science*, 32:594–603, 2005.

[24] H. Zhou and E. Zhu. An elastic-brittle damage constitutive model for modelling cracking of glulam. *World Conference on Timber Engineering*, 34:142–145, 2012.

List of Figures

Appendix A

Future Work

For a complete description of the fracture behavior, additional load cases have to be investigated in future work. As an example, load cases with dominant shear loading are decited in the following.

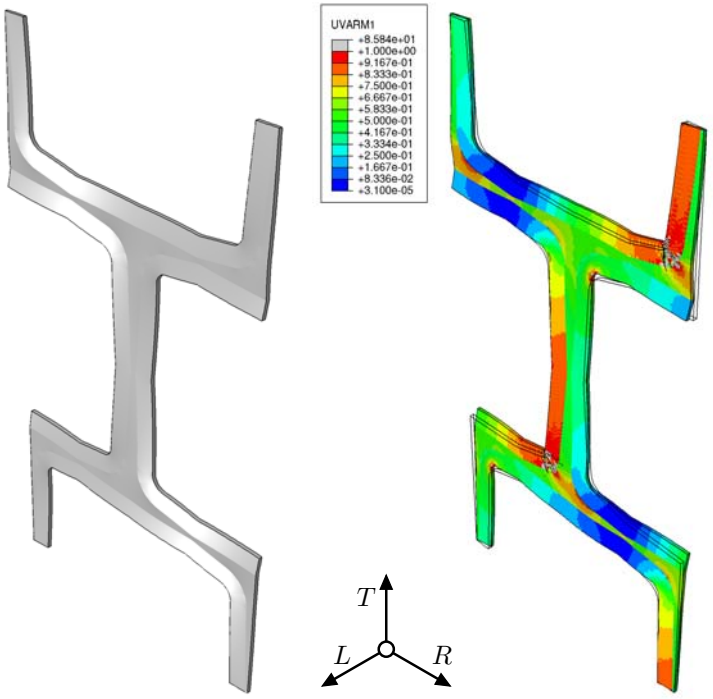

Figure A.1: Initial cracks (on the left) and failure status at last timestep (on the right) due to shear loads in LR and TL-plane

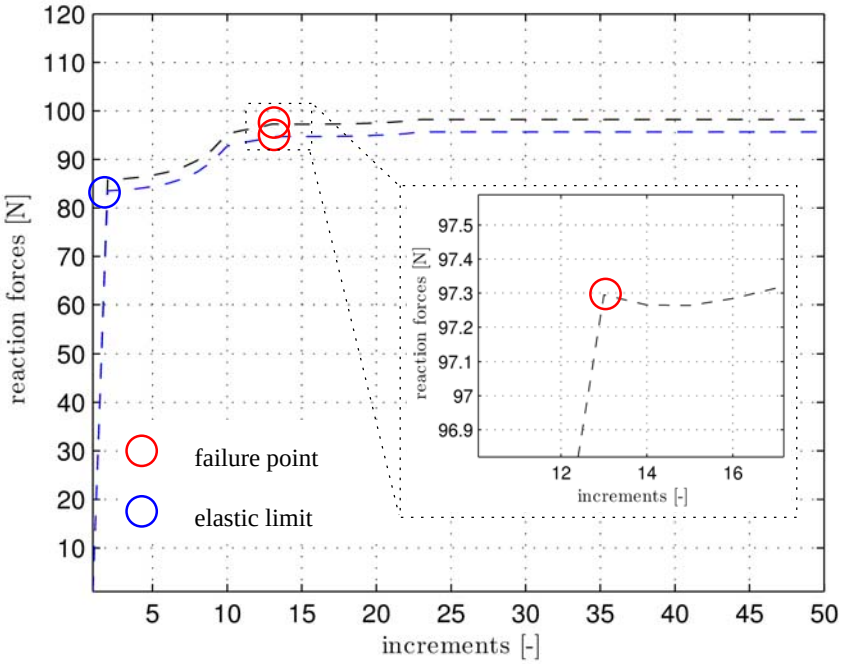

Figure A.2: Reaction forces (RF_L^{NWB} blue and RF_L^{SEB} black line) of an earlywood cell with applied shear load in LR and TL-plane

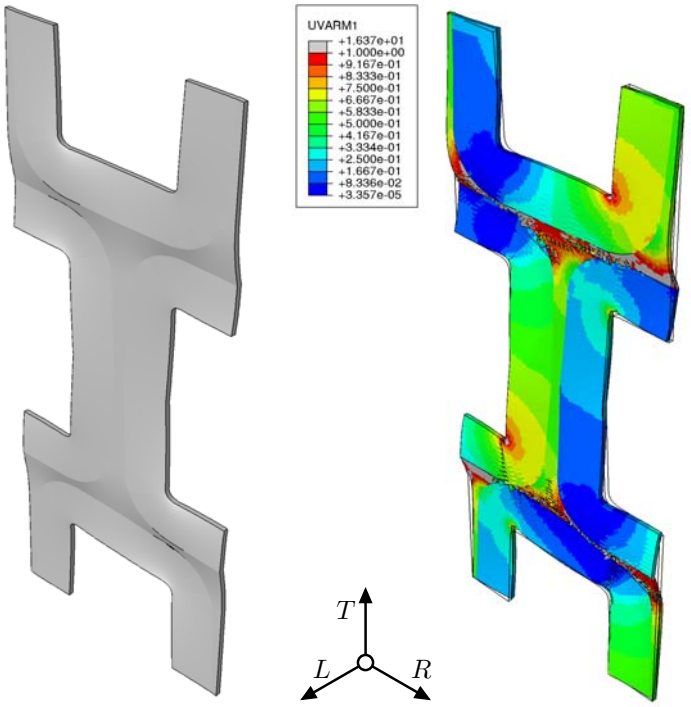

Figure A.3: Initial cracks (on the left) and failure status at last timestep (on the right) due to shear loads in LR and TL-plane

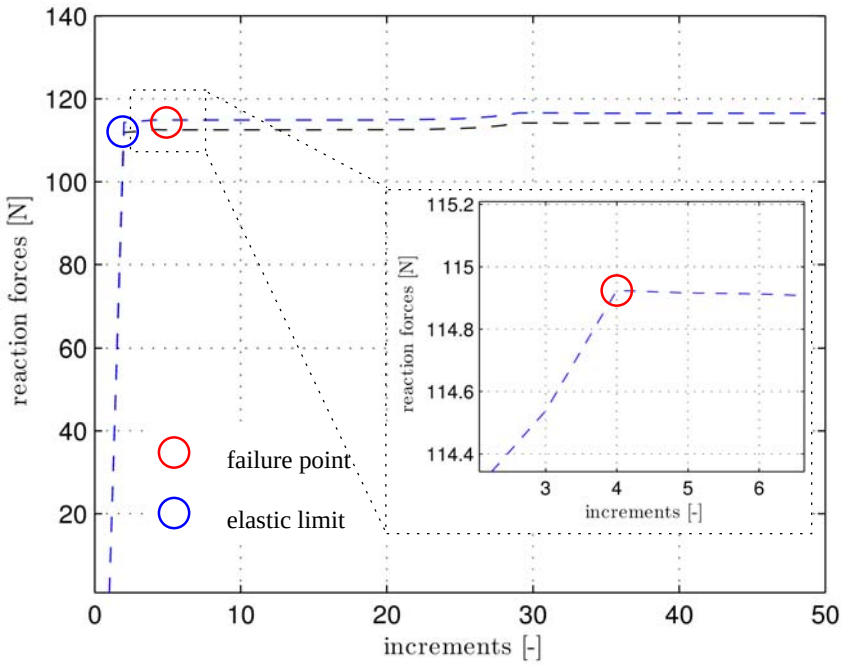

Figure A.4: Reaction forces (RF_L^{NWB} blue and RF_L^{SEB} black line) of a latewood cell with applied shear load in LR and TL-plane

Therefore, additional simulations were done including applied loads in L-direction combined with applied loads in R and/or T-direction. In order to depict a com-

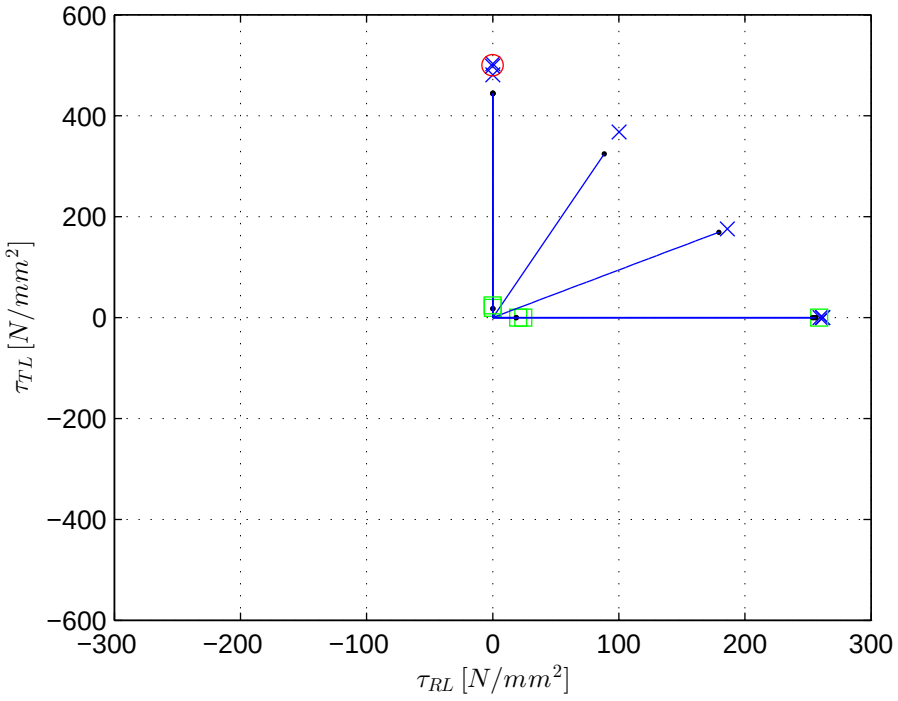

Figure A.5: Stress state at point of failure in τ_{LR}-τ_{RT}-plane of an EW cell

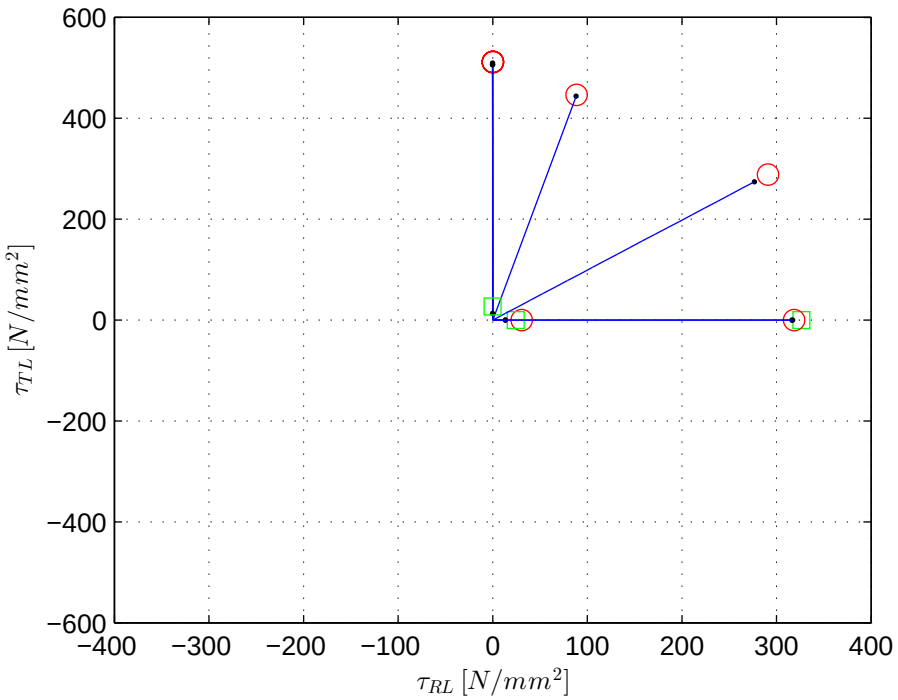

Figure A.6: Stress state at point of failure in τ_{LR}-τ_{RT}-plane of a LW cell

plete failure criterion adequately, however, more simulations with different ratios of these three directions of applied loads will have to be done as well as simulations with additional applied shear laods.

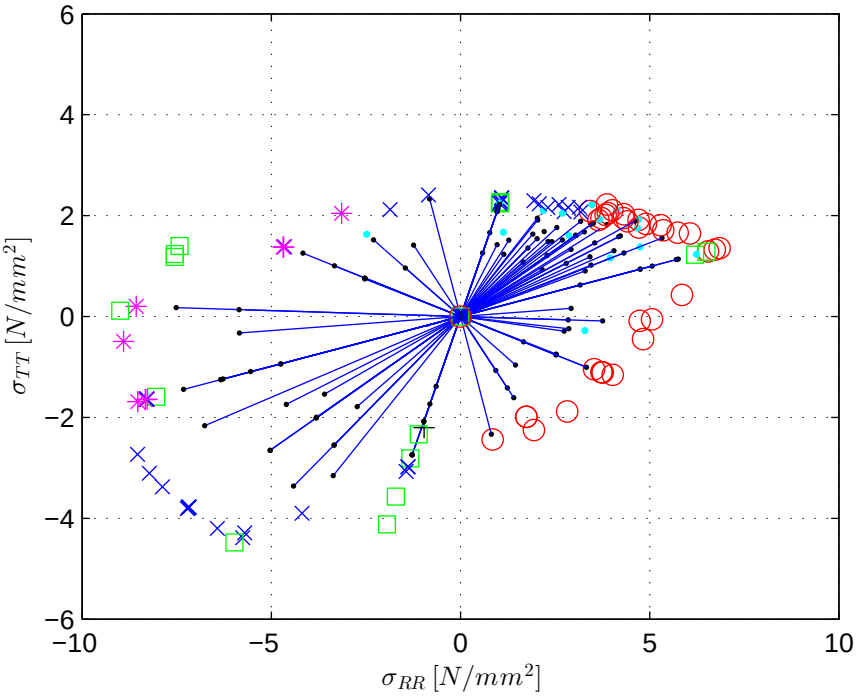

Figure A.7: Stress state at point of failure in σ_{RR}-σ_{TT}-plane of an EW cell

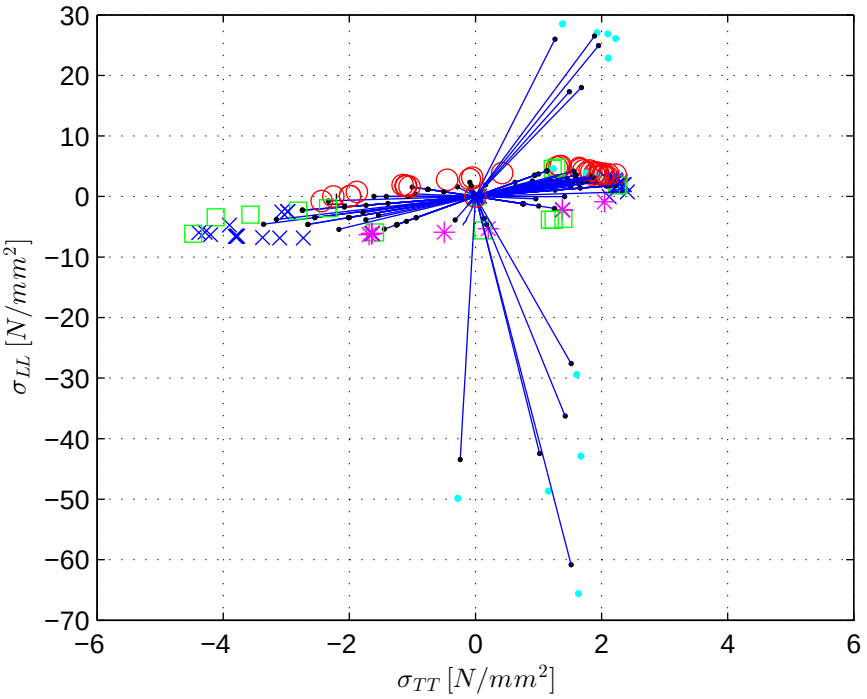

Figure A.8: Stress state at point of failure in σ_{TT}-σ_{LL}-plane of an EW cell

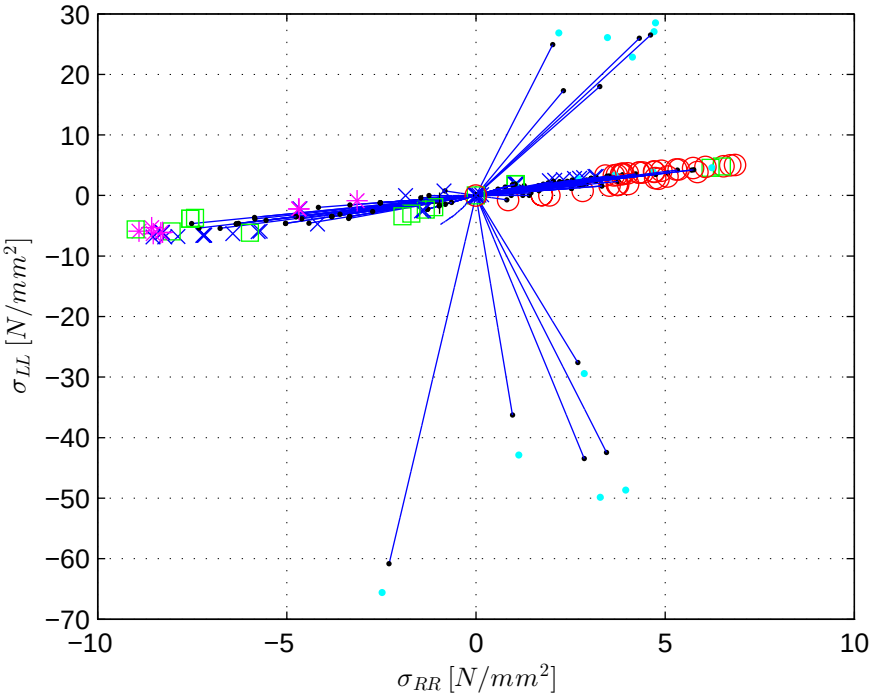

Figure A.9: Stress state at point of failure in σ_{LL}-σ_{RR}-plane of an EW cell

Appendix B

Principle parts of the input file

This appendix contains some abbreviated examplary script files for the simulation tool and an exemplary input file for the FE simulation tool by means of FE software *Abaqus™*. The following code is written in python scripting language and shows how the shape of the unit cell is generated and how the *Abaqus™* input file gets developed. Finally this *Abaqus™* input file can be generated.

Listing B.1: Abaqus input file for finite element solution, uc2.inp

```
1  *Heading
2  ** Job name: uc2 Model name: uc
3  ** Generated by: Abaqus/CAE 6.12-1
4  *Preprint, echo=NO, model=NO, history=NO, contact=NO
5  **
6  ** PARTS
7  **
8  *Part, name=PART-1
9  *Node
10       1,           0.,           0.,          0.5
11       2,  0.281940728,           0.,          0.5
12       3,  0.981317818,   11.4347143,          0.5
13       4,    1.4287833,   13.0432072,          0.5
14       5,   2.49386168,   14.3289309,          0.5
15       6,   3.99099803,   15.0678883,          0.5
16       7,   8.16923237,   16.1270123,          0.5
17       8,   8.54212666,   16.2002525,          0.5
18       9,   8.45787334,   16.7997475,          0.5
19      10,   8.07923603,   16.7673683,          0.5
```

```
34095   34086,   7.53796625,  -18.0011864,         0.25
34096   34087,   7.53070259,  -18.2510815,         0.25
34097   34088,   7.52343893,  -18.5009747,         0.25
34098   34089,    7.8192544,  -17.0094261,         0.25
34099   34090,   7.81174898,  -17.2593136,         0.25
34100   34091,   7.80424309,   -17.509201,         0.25
```

```
  34092,    7.79673767,   -17.7590885,          0.25
  34093,    7.78923178,    -18.008976,          0.25
  34094,    7.78172588,   -18.2588634,          0.25
  34095,    7.77422047,   -18.5087509,          0.25
*Element, type=C3D8R
     1,   439,   438,   268,   267,  6310,  6309,  6182,  6183
     2,     1,   439,   267,     2,   449,  6310,  6183,   442
     3,   436,  5504,   271,   270,  6307, 25455,  6179,  6180
     4,  5731,  5505,  5513,  5732, 25682, 25456, 25464, 25683
     5,   432,   431,  5515,  5513,  6303,  6302, 25466, 25464
     6,  5506,  5509,   430,   429, 25457, 25460,  6301,  6300
     7,  5741,  5740,  5507,  5510, 25692, 25691, 25458, 25461
     8,  5637,  5512,  5729,  5660, 25588, 25463, 25680, 25611
     9,   288,   287,  5527,  5516,  6162,  6163, 25478, 25467
    10,  5609,  5523,  5522,  5426, 25560, 25474, 25473, 25377
```

```
21491, 34094, 34095, 34088, 34087, 25344, 25345, 25338, 25337
21492, 34095, 25346, 25347, 34088, 25345,  5395,  5396, 25338
21493,  1029, 23225, 34089,  7909,    52,  5022, 25339,  1033
21494, 23225, 23226, 34090, 34089,  5022,  5021, 25340, 25339
21495, 23226, 23227, 34091, 34090,  5021,  5020, 25341, 25340
21496, 23227, 23228, 34092, 34091,  5020,  5019, 25342, 25341
21497, 23228, 23229, 34093, 34092,  5019,  5018, 25343, 25342
21498, 23229, 23230, 34094, 34093,  5018,  5017, 25344, 25343
21499, 23230, 23231, 34095, 34094,  5017,  5016, 25345, 25344
21500, 23231,  5023, 25346, 34095,  5016,   249,  5395, 25345
*Elset, elset=_I2, internal, generate
 6897,  6992,     1
*Elset, elset=_I3, internal, generate
 6993,  7072,     1
*Elset, elset=_I4, internal, generate
 7073,  7152,     1
*Elset, elset=_I5, internal, generate
 7153,  7424,     1
*Elset, elset=_I6, internal, generate
 7425,  7472,     1
```

```
*Elset, elset=_PickedSet166, internal, generate
 19981,  20060,      1
*Elset, elset=_PickedSet167, internal, generate
 20061,  20140,      1
*Elset, elset=_PickedSet168, internal, generate
 20141,  20252,      1
*Elset, elset=_PickedSet169, internal, generate
 20253,  20988,      1
*Elset, elset=_PickedSet170, internal, generate
 20989,  21500,      1
** Section: Section-1-_PICKEDSET2_#2
*Solid Section, elset=_PICKEDSET2_#2, material=ML
,
*Orientation, name=Ori-1
-0.963415587779028, -0.268011949779092,          0.,
   0.268011949779092, -0.963415587779028,           0.
1, 15.
```

```
** Section: Section-2-_I2
*Solid Section, elset=_I2, orientation=Ori-1, material=S2
,
*Orientation, name=Ori-2
-0.770090855788788, -0.637934223749199,           0.,
    0.637934223749199, -0.770090855788788,           0.
1, 15.
** Section: Section-3-_I3
*Solid Section, elset=_I3, orientation=Ori-2, material=S2
,
*Orientation, name=Ori-3
-0.442602578437531, -0.896717880696292,           0.,
    0.896717880696292, -0.442602578437531,           0.
1, 15.
** Section: Section-4-_I4
*Solid Section, elset=_I4, orientation=Ori-3, material=S2
,
*Orientation, name=Ori-4
-0.245714496957823, -0.969342243990617,           0.,
    0.969342243990616, -0.245714496957823,           0.
1, 15.
** Section: Section-5-_I5
*Solid Section, elset=_I5, orientation=Ori-4, material=S2
,
```

```
** Section: Section-53-_I53
*Solid Section, elset=_I53, orientation=Ori-52, material=S2
,
*Orientation, name=Ori-53
0.770090855788788, -0.637934223749198,           0.,
    0.637934223749198, 0.770090855788788,           0.
1, 15.
** Section: Section-54-_I54
*Solid Section, elset=_I54, orientation=Ori-53, material=S2
,
*Orientation, name=Ori-54
0.963415587779027, -0.268011949779093,           0.,
    0.268011949779093, 0.963415587779028,           0.
1, 15.
** Section: Section-55-_I55
*Solid Section, elset=_I55, orientation=Ori-54, material=S2
,
*Orientation, name=Ori-55
0.998134794214837, -0.0610486083191458,           0.,
    0.0610486083191458, 0.998134794214837,           0.
1, 15.
** Section: Section-56-_I56
*Solid Section, elset=_I56, orientation=Ori-55, material=S2
,
*Orientation, name=Ori-56
-0.0309908727775955, -0.999519667542607,           0.,
    0.999519667542607, -0.0309908727775955,           0.
1, 15.
** Section: Section-57-_I57
```

```
56169 *Solid Section, elset=_I57, orientation=Ori-56, material=S2
56170 ,
56171 *End Part
56172 **
56173 **
56174 ** ASSEMBLY
56175 **
56176 *Assembly, name=Assembly
56177 **
56178 *Instance, name=PART-1-1, part=PART-1
56179 *End Instance
56180 **
56181 *Nset, nset=ALL_CORNERS, instance=PART-1-1
56182   63,  78,  87,  92, 113, 126, 135, 140
56183 *Nset, nset=NEB, instance=PART-1-1
56184  87,
56185 *Nset, nset=NET, instance=PART-1-1
56186  92,
56187 *Nset, nset=NWB, instance=PART-1-1
56188  113,
56189 *Nset, nset=NWT, instance=PART-1-1
56190  126,
56191 *Nset, nset=SEB, instance=PART-1-1
56192  140,
56193 *Nset, nset=SET, instance=PART-1-1
56194  135,
56195 *Nset, nset=SWB, instance=PART-1-1
56196  78,
56197 *Nset, nset=SWT, instance=PART-1-1
56198  63,
56199 *Nset, nset=EqnSet-1, instance=PART-1-1
56200  135,
56201 *Nset, nset=EqnSet-2, instance=PART-1-1
56202  126,
56203 *Nset, nset=EqnSet-3, instance=PART-1-1
56204  87,
56205 *Nset, nset=EqnSet-4, instance=PART-1-1
56206  92,
56207 *Nset, nset=EqnSet-5, instance=PART-1-1
```

```
204640 *Nset, nset=EqnSet-70184, instance=PART-1-1
204641  10001,
204642 *Nset, nset=EqnSet-70185, instance=PART-1-1
204643  10325,
204644 *Nset, nset=EqnSet-70186, instance=PART-1-1
204645  10000,
204646 *Nset, nset=EqnSet-70187, instance=PART-1-1
204647  109,
204648 *Nset, nset=EqnSet-70188, instance=PART-1-1
204649  100,
204650 ** Constraint: Eqn-1
204651 *Equation
204652 4
204653 EqnSet-1, 3, -1.
```

```
SWT, 3, 1.
SEB, 3, 1.
SWB, 3, -1.
** Constraint: Eqn-2
*Equation
4
EqnSet-2, 3, -1.
SWT, 3, 1.
NWB, 3, 1.
SWB, 3, -1.
** Constraint: Eqn-3
*Equation
4
EqnSet-3, 3, -1.
SEB, 3, 1.
NWB, 3, 1.
SWB, 3, -1.
** Constraint: Eqn-4
*Equation
5
EqnSet-4, 3, -1.
NWB, 3, 1.
SEB, 3, 1.
SWT, 3, 1.
SWB, 3, -2.
```

```
** Constraint: Eqn-35096
*Equation
4
EqnSet-70179, 1, -1.
EqnSet-70180, 1, 1.
SWT, 1, 1.
SWB, 1, -1.
** Constraint: Eqn-35097
*Equation
4
EqnSet-70181, 1, -1.
EqnSet-70182, 1, 1.
SWT, 1, 1.
SWB, 1, -1.
** Constraint: Eqn-35098
*Equation
4
EqnSet-70183, 1, -1.
EqnSet-70184, 1, 1.
SWT, 1, 1.
SWB, 1, -1.
** Constraint: Eqn-35099
*Equation
4
EqnSet-70185, 1, -1.
EqnSet-70186, 1, 1.
SWT, 1, 1.
SWB, 1, -1.
```

```
** Constraint: Eqn-35100
*Equation
4
EqnSet-70187, 1, -1.
EqnSet-70188, 1, 1.
SWT, 1, 1.
SWB, 1, -1.
**
** include material, failure, load definitions
**
*INCLUDE, INPUT=000_bcmat.inp
**
```

The previous input file needs some more definitions. In this short remaining part of the input file, the missing definitions for the used materials like strength values, stiffnesses and the loads get introduced.

Listing B.2: Abaqus input file including the material and load definitions, 000_bcmat.inp

```
**Enrichment, name=ML, type=PROPAGATION CRACK, elset=ML
**Enrichment, name=S2, type=PROPAGATION CRACK, elset=S2
**
**
*Enrichment, name=S2-0, type=PROPAGATION CRACK, elset=S2-vier-0
*Enrichment, name=S2-1, type=PROPAGATION CRACK, elset=S2-vier-1
**Enrichment, name=S2-2, type=PROPAGATION CRACK, elset=S2-vier-2
**Enrichment, name=S2-3, type=PROPAGATION CRACK, elset=S2-vier-3
**
**
*Enrichment, name=Crack-0, type=PROPAGATION CRACK, elset=Cset-0
*Enrichment, name=Crack-1, type=PROPAGATION CRACK, elset=Cset-1
*Enrichment, name=Crack-2, type=PROPAGATION CRACK, elset=Cset-2
*Enrichment, name=Crack-3, type=PROPAGATION CRACK, elset=Cset-3
*Enrichment, name=Crack-4, type=PROPAGATION CRACK, elset=Cset-4
*Enrichment, name=Crack-5, type=PROPAGATION CRACK, elset=Cset-5
*Enrichment, name=Crack-6, type=PROPAGATION CRACK, elset=Cset-6
*Enrichment, name=Crack-7, type=PROPAGATION CRACK, elset=Cset-7
**
**
*End Assembly
**
*Material, name=ML
*User Output Variables
      1,
*Elastic, type=ISOTROPIC
 5927.7, 0.3157
*Damage Initiation, criterion=USER, PROPERTIES=3, FAILURE
   MECHANISMS=1, TOLERANCE=0.01
** Prop1=tauy, Prop2=mue, Prop3=(udmgini.f file destinction - if
   0.0 it will be used, else not)
14.3, 0.0, 0.0
*Damage Evolution, FAILURE INDEX=1, type=DISPLACEMENT, mode mix
   ratio=TRACTION
 0.00001
```

```
*DAMAGE STABILIZATION
 1.e-4
**
*Material, name=S2
*User Output Variables
      1,
*Elastic, type=ORTHOTROPIC
 38212, 20744, 38212, 14632, 14632, 230344, 7908, 7908
      8732
*Damage Initiation, criterion=USER, PROPERTIES=3, FAILURE
   MECHANISMS=3, TOLERANCE=0.01
 175, 60, 35
*Damage Evolution, FAILURE INDEX=1, type=DISPLACEMENT, mode mix
   ratio=TRACTION
 0.00001,
*Damage Evolution, FAILURE INDEX=2, type=DISPLACEMENT, mode mix
   ratio=TRACTION
 0.0001,
*Damage Evolution, FAILURE INDEX=3, type=DISPLACEMENT, mode mix
   ratio=TRACTION
 0.0001,
*DAMAGE STABILIZATION
 1.e-3
**
*Time Points, name=TimePoints-1, GENERATE
0., 1., 0.01
**
** STEP: Step-1
**
*Step, name=Step-1, inc=10000
*Static
0.01, 1., 1e-20, 0.01
**
** CONTROLS
**
*Controls, reset
*Controls, parameters=time incrementation
10, 10, 25, 40, 10, , , 20, 10, ,
**, , 25, 40, 6, , , 20, 7, ,
*Controls, parameters=constraints
1.e-3, 1.e-3, 1.e-3
**
** BOUNDARY CONDITIONS
**
*Boundary, op=NEW
SWB, 1, 1
*Boundary, op=NEW
SWB, 2, 2
*Boundary, op=NEW
SWB, 3, 3
*Boundary, op=NEW
SEB, 3, 3
*Boundary, op=NEW
NWB, 3, 3
```

```
*Boundary, op=NEW
SWT, 1, 1
*Boundary, op=NEW
SWT, 2, 2
*Boundary, op=NEW
SWT, 3, 3
**
** change u_R-SEB, u_R-NWB, u_T-SEB, u_T-NWB for different
   loadcases
**
*Boundary, op=NEW
SEB, 1, 1, u_R-SEB
*Boundary, op=NEW
NWB, 1, 1, u_R-NWB
*Boundary, op=NEW
SEB, 2, 2, u_T-SEB
*Boundary, op=NEW
NWB, 2, 2, u_T-NWB
**
** OUTPUT REQUESTS
**
*Restart, write, frequency=0
*Print, solve=NO
**
** FIELD OUTPUT: F-Output-2
**
*Output, field
*Element Output, directions=YES
E, S, STATUSXFEM, UVARM
**
** FIELD OUTPUT: F-Output-1
**
*Node Output
PHILSM, PSILSM, RF, U
**
** HISTORY OUTPUT: H-Output-1
**
*Output, history, variable=PRESELECT
*End Step
```